


Article

Implementation Process Simulation and Performance Analysis for the Multi-Timescale Lookup-Table-Based Maximum Power Point Tracking under Variable Irregular Waves

Xuhui Yue ^{1,2,*} , Feifeng Meng ^{1,2}, Zhoubo Tong ^{1,2}, Qijuan Chen ³, Dazhou Geng ⁴ and Jiaying Liu ^{1,2}

¹ PowerChina HuaDong Engineering Corporation Limited, Hangzhou 311122, China; meng_ff@hdec.com (F.M.); tong_zb@hdec.com (Z.T.); liu_jy5@hdec.com (J.L.)

² Hangzhou Huachen Electric Power Control Corporation Limited, Hangzhou 311122, China

³ Key Laboratory of Transients in Hydraulic Machinery, Ministry of Education, Wuhan University, Wuhan 430072, China; qjchen@whu.edu.cn

⁴ China Renewable Energy Engineering Institute, Beijing 100120, China; gengdz@creei.cn

* Correspondence: yue_xh@hdec.com; Tel.: +86-0571-56623055

Abstract: The efficacy of the multi-timescale lookup-table-based maximum power point tracking (MLTB MPPT) in capturing energy at various fixed sea states has already been demonstrated. However, it remains imperative to conduct a more comprehensive evaluation of the MPPT tracking performance under varying sea states in practical scenarios. Additionally, it is crucial to engage in an in-depth analysis of the dynamic process and energy loss/consumption associated with MLTB MPPT implementations. This paper focuses on the implementation process simulation and performance analysis for the MLTB MPPT under variable irregular waves. Firstly, the structure of the wave power controller based on a MLTB MPPT algorithm is described in detail, as well as that of a controlled plant, known as a novel inverse-pendulum wave energy converter (NIPWEC). Secondly, mathematical models for the MLTB MPPT are developed, taking into account the efficiency of each link. In this paper, we present simplified modelling methods for both permanent magnet synchronous generator (PMSG) vector control and permanent magnet synchronous motor (PMSM) servo control. Finally, the tracking performance of the MLTB MPPT in the presence of variable irregular waves is comprehensively analyzed by simulating the implementation process and comparing it with two other MPPT algorithms, i.e., the frequency- and amplitude-control-based MPPT and the lookup-table-based internal mass position adjustment combined with the optimal fixed damping search. Results show that the MLTB MPPT (Method 2) is a competitive algorithm. Besides, a significant portion (>12%) of the time-averaged absorbed power is actually lost during the power generation process. On the other hand, the power required for a mass-position-adjusting mechanism is relatively small (approximately 0.2 kW, <1.5%). The research findings can offer theoretical guidance for optimizing the operation of NIPWEC engineering prototypes under actual sea conditions.

Keywords: wave energy converter; maximum power point tracking; multi-timescale lookup table; PMSG vector control; PMSM servo control; variable irregular waves



Citation: Yue, X.; Meng, F.; Tong, Z.; Chen, Q.; Geng, D.; Liu, J. Implementation Process Simulation and Performance Analysis for the Multi-Timescale Lookup-Table-Based Maximum Power Point Tracking under Variable Irregular Waves. *Energies* **2023**, *16*, 7501. <https://doi.org/10.3390/en16227501>

Academic Editors: Eugen Rusu, Mehdi Neshat and Soheil Esmaeilzadeh

Received: 7 September 2023

Revised: 29 October 2023

Accepted: 7 November 2023

Published: 9 November 2023



Copyright: © 2023 by the authors. Licensee MDPI, Basel, Switzerland. This article is an open access article distributed under the terms and conditions of the Creative Commons Attribution (CC BY) license (<https://creativecommons.org/licenses/by/4.0/>).

1. Introduction

Despite the abundance of wave energy on the global ocean surface, the wave-by-wave, hour-by-hour, and site-by-site variations of wave power level are still the main factor that prevents wave energy utilization (WEU) technology from converging and maturing [1]. In 2020, the active wave capacity was recorded at 2.31 MW [2], which is substantially lower than expectations. The majority of WEU programs are currently in the prototype demonstration stages of wave energy converters (WECs). Besides, plenty of them have unfortunately failed due to technical or commercial challenges. This reality means that a significant portion of wave energy still lies in an untapped condition.

In order to enhance the WEC energy capture capacity under wave power level variations, numerous control methods have been proposed by researchers. These methods include latching control [3,4], model predictive control [5,6], natural period control methods (NPCMs), and maximum power point tracking (MPPT) technologies. Given that the primary focus of this paper revolves around NPCMs and MPPT technologies, their development processes and current research status are introduced below.

NPCMs are the slow-tuning approaches to achieve resonance between WECs and ocean waves. This resonance occurs when the natural period/frequency of a WEC matches that of an incident wave. In the resonant state, WECs are supposed to capture the most wave energy and generate an extra amount of electricity. To date, many innovative mechanical structures have been developed with the aim of implementing natural period control. Most of them are predicated on the inherent inertia/stiffness adjustment. In 1975, Budar and Falnes [7] introduced the concept of a resonant point absorber, whose natural period can be changed to the wave characteristic period by adjusting the inertia moment of a flywheel. In 2010, Costa et al. [8] presented a wave energy hyperbaric converter, wherein an oscillating body is connected to a hyperbaric chamber via a lever arm. Herein, the oscillating body's inertia can be altered via a sliding mass on the lever arm. Flocard and Finnigan [9] developed a cylindrical bottom-hinged point absorber, which can modify its inertia by selectively filling compartments with water. The experimental study demonstrated that a 15–25% increase in power capture can be obtained, compared to a constant inertia configuration. Subsequently, Marei et al. [10] researched an Archimedes wave swing with adjustable stiffness level whose air pressure and volume can be changed to achieve resonance. Finally, in recent years, Têtu et al. [11] installed a negative spring mechanism on the Wavestar setup to shift the resonance period. Temiz et al. [12] changed the ballast inertia moment by altering ballast compartment locations and mass properties, so as to achieve different resonance frequencies of a pitching WEC. In recent studies, movable mass methods have been introduced to solo Duck WECs [13] or inverse pendulum-type wave energy converters [14–17] in order to achieve hydrostatic stiffness adjustment and resonant energy capture.

MPPT technologies have been widely utilized for the renewable power enhancement. For WEU, they have plenty of application scenarios, such as the power conversion components [18–23], the hydraulic transmission devices [24,25], the latching mechanisms [26], and even the mechanisms for natural period control [10,14,17]. From 2009 to 2012, Amon et al. [18–20] first implemented diverse fixed-step perturbation and observation (P&O) algorithms on the duty ratio of a buck converter and the phase resistance/impedance of a three-phase pulse-width modulation (PWM) rectifier in order to maximize the WEC output power. In 2016, Ding et al. [25] and Hardy et al. [26] applied two other fixed-step P&O algorithms to the load damping tuning of a hydraulic power take-off (PTO) as well as the latching time optimization of an oscillating water column, respectively. The MPPT tracking performance under variable irregular waves, i.e., the sea states with changeable parameters, was also discussed in [25,26]. The cycling MPPT algorithm, which incorporates an adjustable resistance load, was introduced by Lettenmaier et al. [27]. The performance of this algorithm was demonstrated by the sea trials of a half-scale prototype and time-domain simulations at changing sea states. Recently, there has been an increasing interest among researchers in investigating MPPT technologies. Numerous algorithms, such as the fast-tracking fractional open circuit voltage MPPT [28], the segmental fixed-step P&O [24], the variable-step P&O [21,22,29], the lookup-table-based MPPT [22,30], and the heuristic-algorithm-based MPPT [23,31] have emerged. To conclude, the existing MPPT technologies possess the following three features:

(1) Control variables of MPPT are diverse. The diversity of control variables is caused by the fact that MPPT can be implemented via different actuators. Since MPPT mainly focuses on algorithms, its application could be unlimited by hardware configuration. Therefore, MPPT actuators can involve buck/boost/buck-boost converters [18–22], three-phase PWM rectifiers [14,17–20], and hydraulic PTOs [24,25], etc. Different actuators lead

to different control variables. Nowadays, control variable families include the duty ratio [18–22], the electric impedance [18], the equivalent mechanical impedance [23], the resistance/damping [14,17,19,20,25,27,29], and the fractional displacement of a hydraulic motor [24].

(2) The update of durations of MPPT can range from the millisecond level to the kilo-second level. In terms of the duty ratio/electric impedance/resistance for a three-phase PWM rectifier, the lower bounds of the investigated update duration can reach 0.001 s [18–20]. However, for load damping of a hydraulic PTO, the researched update duration is 4620 s [25].

(3) The majority of MPPT technologies involve electrical machine control. MPPT technologies can be applied to linear-generator control [10,18–20], wound rotor induction generator control [30], and permanent magnet synchronous generator (PMSG) control [14,17,22,23].

The aforementioned features reveal that the control variable and update duration for a WEC MPPT technology can be selected with few constraints, as long as the MPPT performance is reliably ensured.

This paper focuses on novel inverse-pendulum WECs (NIPWECs), i.e., a kind of inverse-pendulum-type WECs which include movable internal masses to achieve resonance. The fundamental framework of a NIPWEC was first proposed by Cai et al. [15,16]. Dong et al. [14] combined the internal mass adjustment with PTO damping tuning and put forward frequency and amplitude control based (FACB) MPPT. The term “frequency control” pertains to the adjustment of the internal mass position in order to achieve resonance. On the other hand, “amplitude control” involves tuning the PTO damping to align with the amplitude of the NIPWEC inherent impedance. Herein, the inherent impedance under an irregular wave can be calculated as the weighted average of the corresponding ones under regular waves. Moreover, the update duration of the FACB MPPT appears to be a minimum of several hundreds of seconds. This is because both frequency control and amplitude control depend on the frequency domain analysis of the wave excitation force signal over the past few hundreds of seconds. Furthermore, Zheng et al. [17] and Yue et al. [32] proposed multi-timescale lookup-table-based (MLTB) MPPT. It involves altering the internal mass position via a 1-dimensional (1-D) resonant position table and tuning the PTO damping via a 2-D optimal PTO damping table. The first table can be obtained in advance by a frequency domain analysis, while the second table can be achieved beforehand using the regular wave simulations. The update duration of MLTB MPPT depends on the quantity of individual waves n_w . If $n_w = 1$, the update duration can reach the second level. The fundamental distinction between FACB MPPT and MLTB MPPT is that they choose different mathematical models to obtain the optimal PTO damping. FACB MPPT utilizes a frequency domain model to directly compute the optimal PTO damping, whereas MLTB MPPT inquires an optimal PTO damping table obtained through a series of simulations based on a time-domain model. Since calculations in the frequency domain cannot reliably include the really existing nonlinear forces, such as an endstop moment and a sine function hydrostatic restoring moment, compared to the simulations in the time domain, MLTB MPPT may appear more reliable and may possess greater potential for searching the real maximum power point. It should be noted that the NIPWEC in this manuscript is considered to be completely submerged in seawater to avoid the influence of the displacement changes on the hydrostatic restoring moment. Further performance comparison of the two MPPT algorithms will be discussed in Section 4.3.3.

The efficacy of MLTB MPPT in capturing energy at various fixed sea states has already been demonstrated by Ref. [32]. Since the real irregular wave environment is variable, it is still necessary to further assess the MPPT tracking performance at changing sea states. The highlights of this paper are outlined as below.

(1) Mathematical models of the PMSG vector control and permanent magnet synchronous motor (PMSM) servo control are established for the MLTB MPPT. The models contain the efficiency values of the key links of the PTO damping tuning and internal mass

position adjustment. Hence, they can be utilized to simulate the changing control signals, the controlled dynamic process of the inverse pendulum, PTO and mass-position-adjusting mechanism (MPAM), as well as the power transmission/loss/consumption at each link.

(2) Maximum absorbed power tracking performance of the MLTB MPPT in changing sea states is comprehensively investigated via comparison with two other MPPT algorithms, i.e., the FACB MPPT and the lookup-table-based internal mass position adjustment (LTB IPA) combined with the optimal fixed damping search (OFDS).

The subsequent sections of this paper are organized as follows. First of all, the system structure, control flow, and mathematical models of the MLTB MPPT for a NIPWEC are presented in Section 2. Then, the parameter configuration and simulation settings for time-domain simulations are detailed in Section 3. Afterwards, the MLTB MPPT tracking performance under variable irregular waves is investigated in Section 4. Lastly, the main findings are ultimately summarized in Section 5.

2. MLTB MPPT for a NIPWEC: Structure, Control Flow, and Mathematical Models

2.1. Overall Structure

Figure 1 illustrates the structure diagram of a NIPWEC and the wave power controller with a MLTB MPPT algorithm. Herein, the characteristic period T_c means the wave period which is derived from the wave energy spectrum, such as the energy period T_e or the peak period T_p . The NIPWEC consists of an inverse pendulum, a speed-increase mechanism, a PMSG, a MPAM, and a three-phase PWM rectifier. At first, the inverse pendulum is uninterruptedly driven by the wave excitation moment M_E . Next, the speed-increase mechanism accelerates the swing process and transmits the kinetic energy from the inverse-pendulum to a PMSG. At last, the PMSG absorbs the above kinetic energy and generates electricity for a direct current (DC) bus.

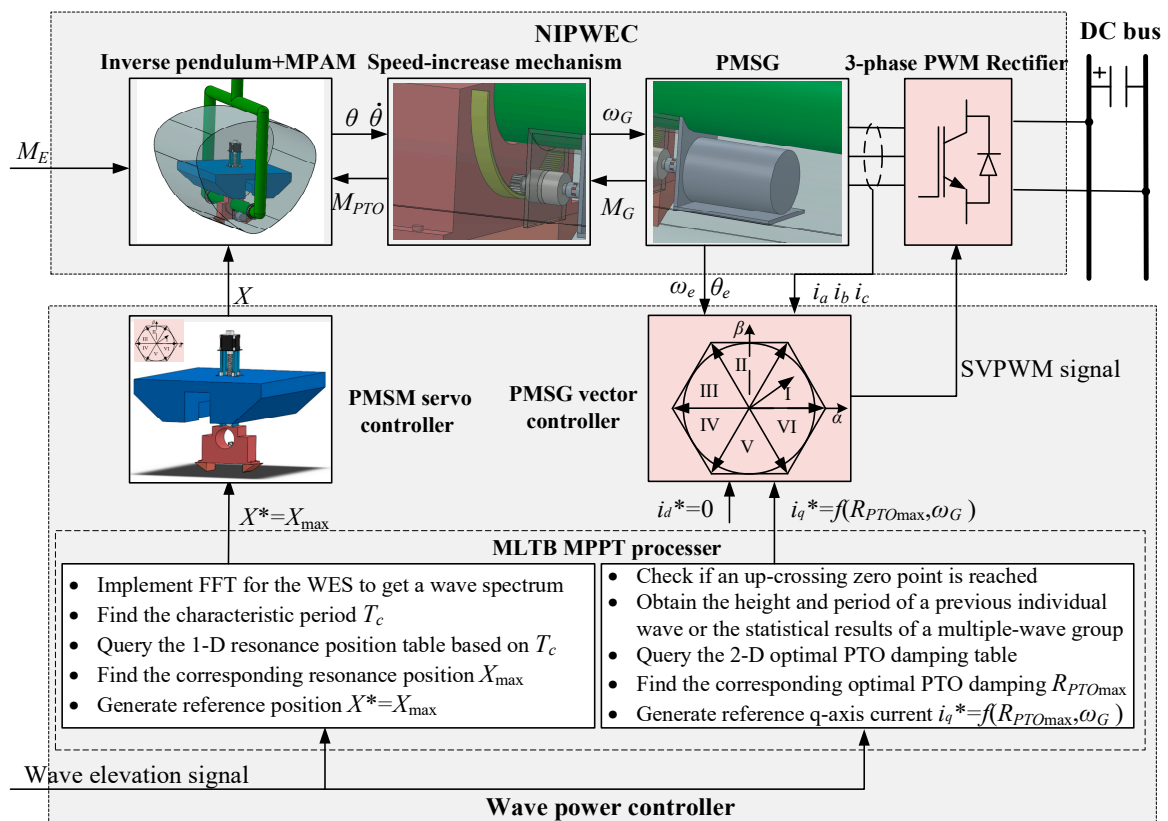


Figure 1. Structure diagram of the NIPWEC and the wave power controller with a MLTB MPPT algorithm.

In addition, MPAM contains a permanent magnet synchronous motor (PMSM), a reduction gearbox, a ball screw, and a moveable internal mass. Reduction gearbox decelerates the rotation of a PMSM and drives the coaxially connected ball screw to rotate slowly. Then, the ball screw raises or downgrades the internal mass to the given position.

Furthermore, the wave power controller contains a MLTB MPPT processor, a PMSM servo controller, and a PMSG vector controller. The working principle of a wave power controller is as follows. Firstly, wave elevation signals (WESs) are collected and inputted into a MLTB MPPT processor. Next, the MLTB MPPT processor queries a 1-D resonance position table or a 2-D optimal PTO damping table and identifies the corresponding resonance position X_{\max} or the optimal PTO damping $R_{PTO\max}$, according to the results from the spectral analysis and statistical analysis of WESs. Then, the PMSM servo controller ensures MPAM trails the reference position $X^* = X_{\max}$. Meanwhile, the PMSG vector controller carries out 0 d -axis current (i_d) control and changes the q -axis current i_q to track the reference q -axis current $i_q^* = f(R_{PTO\max}, \omega_G)$. Herein, ω_G signifies the angular velocity of the PMSG rotor. Finally, NIPWEC is controlled to ensure it fully absorbs wave power in the resonant state. Detailed description of the MLTB MPPT processor can be seen in Section 2.2. More information on the PMSG vector controller or the PMSM servo controller is displayed in Section 2.3.

2.2. Control Flow of MLTB MPPT

For the aforementioned NIPWEC, the maximum power point (MPP) under a regular wave can be easily found via a series of time-domain tests against different internal mass positions and PTO damping (R_{PTO}) values. The resonance position X_{\max} and optimal PTO damping $R_{PTO\max}$ corresponding to the MPP of a specific regular wave are fixed and scarcely affected by the selection of time windows. Hence, it is worth regarding X_{\max} and $R_{PTO\max}$ as two NIPWEC feature parameters, and creating two lookup tables, i.e., a 1-D resonance position table and a 2-D optimal PTO damping table, for the operation guidance.

The real ocean waves are irregular waves. Compared with regular waves, wave power carried by each individual wave, i.e., the wave elevation within two adjacent up-crossing zero points, in an irregular wave sequence is constantly changing. Therefore, it is difficult to find a universally applicable MPP during different time windows. This problem is prominent especially for short time windows. Additionally, irregular waves with the same characteristic period and characteristic height may possess different MPPs during the uniform time window, since the wave spectrum density function of each irregular wave sequence is uncertain. To sum up, the comprehensive search for the fixed MPPs of diverse irregular waves, analogous to the process for regular waves, is meaningless for operation optimization. Herein, MLTB MPPT applies the two lookup tables of the NIPWEC feature parameters X_{\max} and $R_{PTO\max}$ to the real-time operation optimization under irregular waves. It can avoid the complex, comprehensive search and make the real-time tracking reasonable and reliable.

MLTB MPPT processor owns two modules. The first one is a i_q^* generating module for the lookup-table-based (LTB) PTO damping tuning. Control flow of this module can be seen in Figures 2 and 3. The i_q^* generating module is divided into two parts depending on whether the quantity of individual waves $n_w > 1$. If yes, a time-domain statistic will be calculated for both the height H_{n_w} and period T_{n_w} of the previous n_w individual waves, for the sake of the $R_{PTO\max}$ query. Otherwise, the height H_n and period T_n of the previous (n -th) individual wave will be directly utilized to query $R_{PTO\max}$. Herein, i_q^* is generated according to the following equation:

$$i_q^* = f(R_{PTO\max}, \omega_G) = -\frac{R_{PTO\max}\omega_G}{1.5n_p\phi_f k_2^2} \quad (1)$$

where n_p is the pole-pair number, ϕ_f is the rotor flux, and k_2 is the acceleration ratio of the speed-increase mechanism.

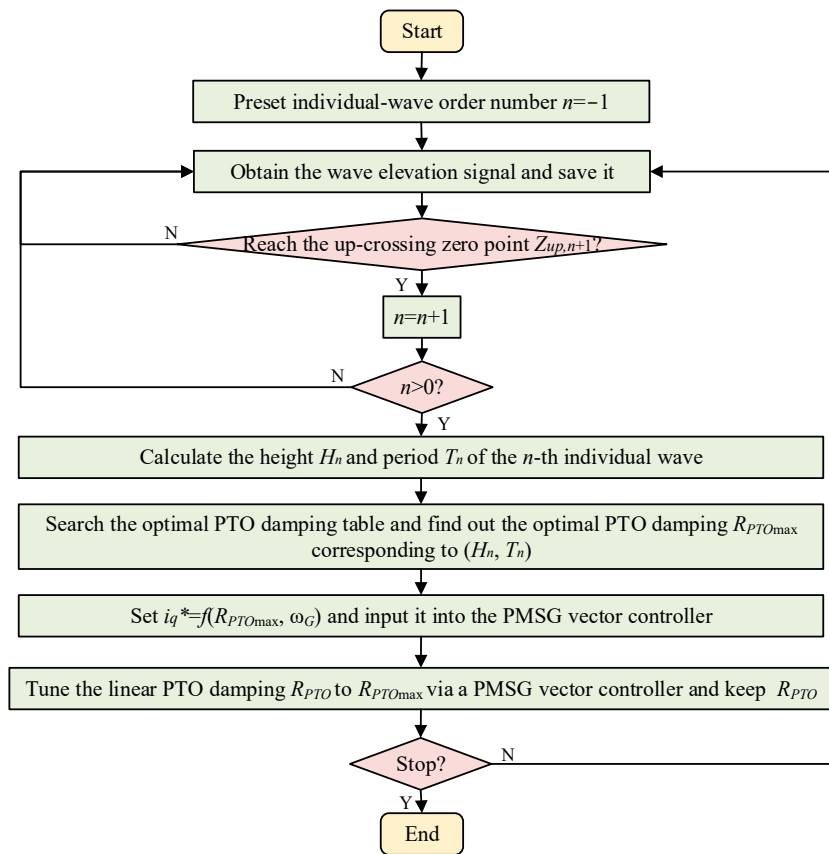


Figure 2. Flow chart of the LTB PTO damping tuning based on an i_q^* generating module ($n_w = 1$).

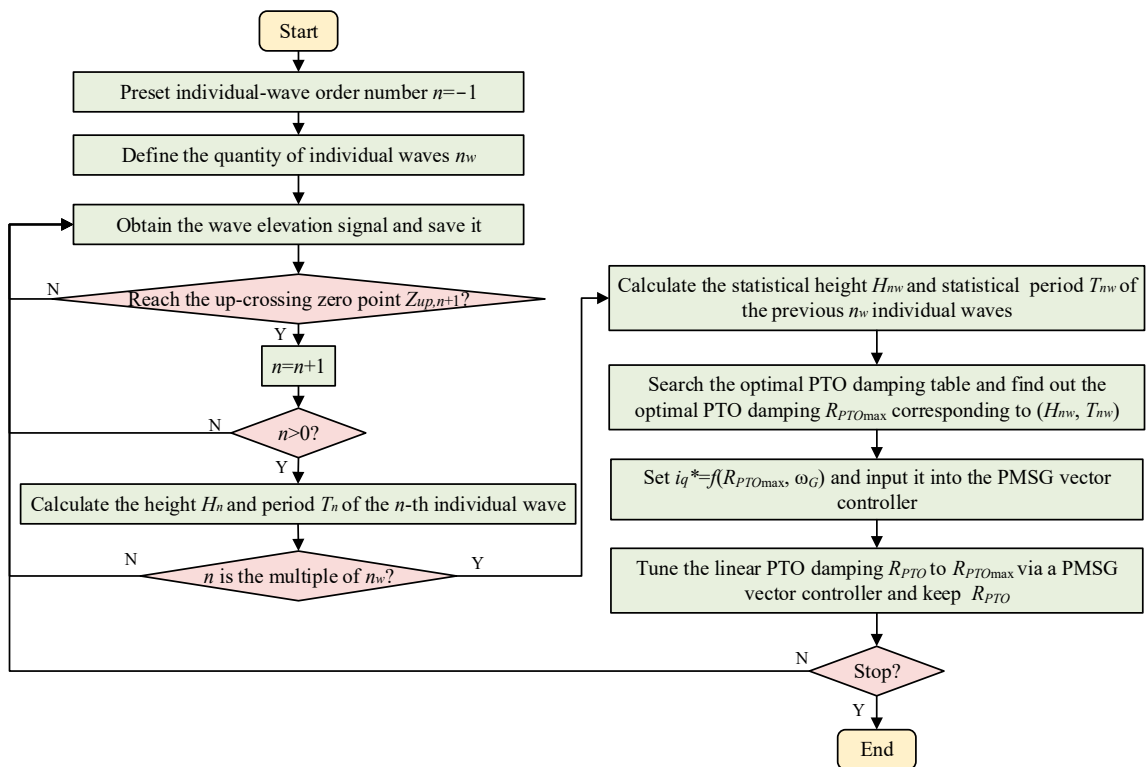


Figure 3. Flow chart of the LTB PTO damping tuning based on an i_q^* generating module ($n_w > 1$).

Here, we consider two obtainment methods for (H_{n_w}, T_{n_w}) . Method 1: calculate the mean height $H_{m,1/3}$ and mean period $T_{m,1/3}$ for the first one-third individual waves of the multiple-wave group, which is rearranged in a descending order of wave heights, and take $(H_{m,1/3}, T_{m,1/3})$ as (H_{n_w}, T_{n_w}) [22,32]. Method 2: calculate the mean height H_m and mean period T_m for all individual waves of the multiple-wave group and take (H_m, T_m) as (H_{n_w}, T_{n_w}) .

The second module is named an X^* generating module for the LTB IPA. The control flow of this module can be seen in Figure 4. First, implement a fast Fourier transformation (FFT) for the WES to get a wave spectrum. Next, find the characteristic period T_c of the wave spectrum. Then, query the 1-D resonance position table based on T_c and determine the corresponding X_{\max} . Finally, generate $X^* = X_{\max}$ and implement PMSM servo control. According to Ref. [32], energy period resonance delivers a good power absorption performance and possesses high reliability. Hence, we take the energy period T_e , i.e., the ratio between the moments of order -1 and 0 of a wave spectrum, as the T_c here.

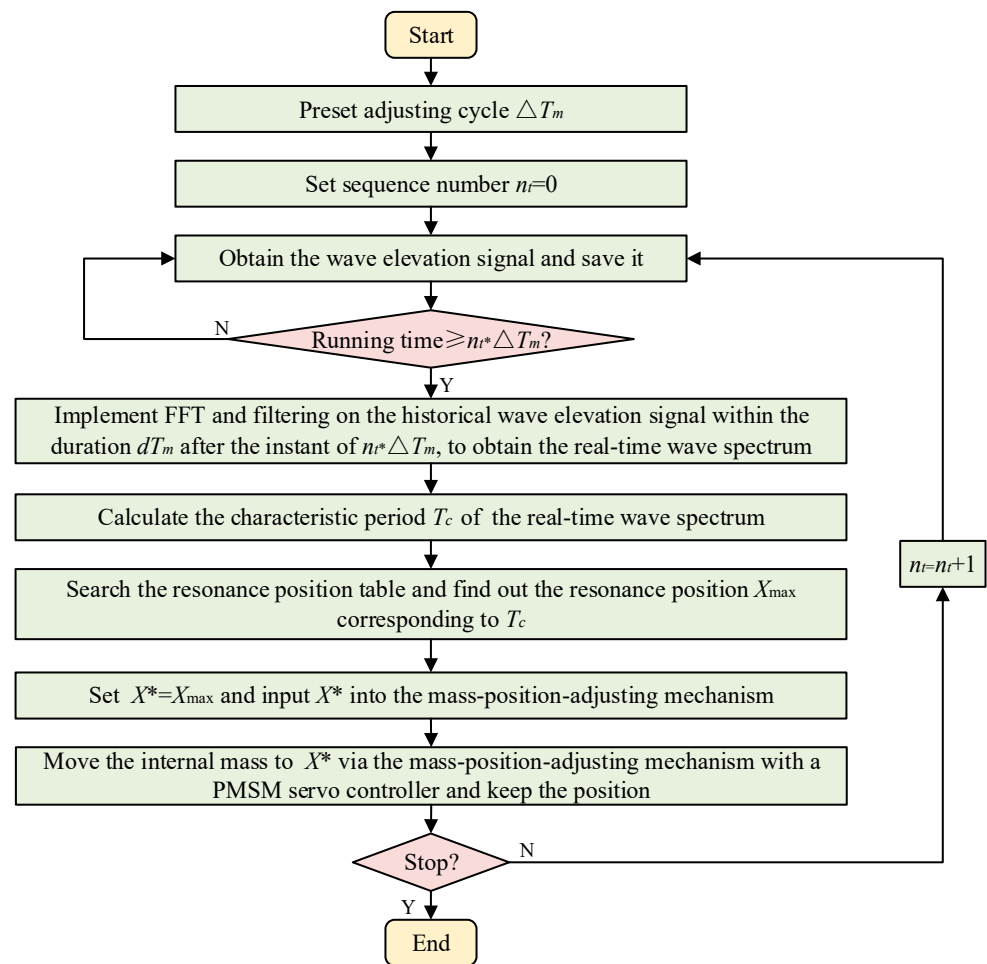


Figure 4. Flow chart of the LTB internal mass position adjustment based on an X^* generating module.

2.3. Mathematical Models for MLTB MPPT

2.3.1. Mathematical Models of the PMSG Vector Control for LTB PTO Damping Tuning

The PMSG vector controller for PTO damping tuning was based on the 0 d -axis current control. It only contained a current loop proportional–integral (PI) regulator. The general model (GM) of the PMSG vector control can be seen in Refs. [14,33]. However, GM is complicated and adverse to fast solving since sub-models of the space vector PWM (SVPWM) and rectifier thyristors are comprehensively included in this model. This disadvantage is especially evident for the simulations of a long timescale, such as the kilo-second timescale

simulations for changing sea states. Therefore, it is necessary to propose a simplified model (SM) of the PMSG vector control in order to reduce the computational burden. Sjolte et al. [34] regarded PWM and converter as a unity gain for the preliminary discussion of PMSG vector control. Herein, we present an SM which adopts the same simplification and assumes that the reference d -axis current $i_d^* = 0$ has been well tracked. This means that the i_q control can be decoupled from the i_d control, eliminating the time-consuming power electronic simulations. Although the SM idealizes the power electronic control and cannot simulate the high-frequency components caused by chopping, it can effectively emulate the long-term trends of key variables, e.g., i_q , the PTO moment M_{PTO} , and the absorbed power P_{PTO} . This is enough for our research. In order to further validate the simplification feasibility, the performance comparison between the GM and the proposed SM is discussed in Section 4.1.

A block diagram of the PMSG vector control can be seen in Figure 5. Mathematical models of key links are displayed as below.

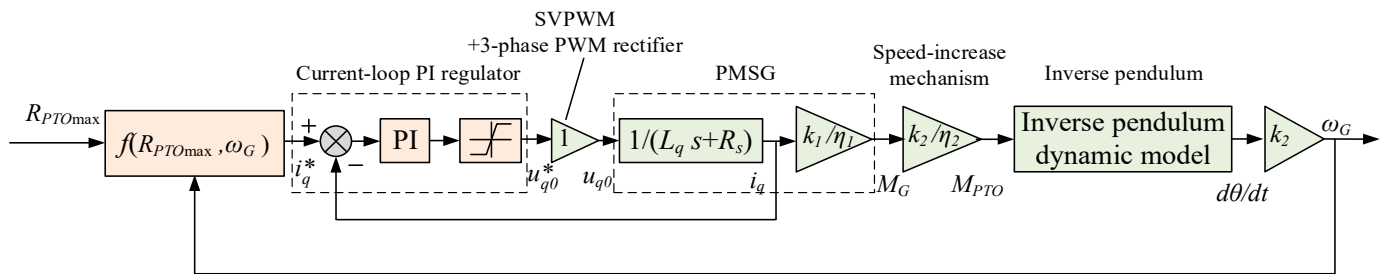


Figure 5. Block diagram of the PMSG vector control for LTB PTO damping tuning.

The PMSG current loop PI regulator is expressed as:

$$u_{q0}^* = \begin{cases} \left(K_{q-p} + \frac{K_{q-i}}{s} \right) (i_q^* - i_q), & |u_{q0}^*| \leq u_{q0max}^* \\ \text{sgn}(u_{q0}^*) u_{q0max}^*, & |u_{q0}^*| > u_{q0max}^* \end{cases} \quad (2)$$

where u_{q0}^* is the reference q -axis voltage without the feedforward decoupling, K_{q-p}/K_{q-i} is the proportional/integral coefficient, u_{q0max}^* is the upper bound of u_{q0}^* , and sgn is the symbolic function.

The PMSG model is as follows:

$$\begin{cases} i_q = \frac{u_q - \phi_f n_p \omega_G}{L_q s + R_s} = \frac{u_{q0}}{L_q s + R_s} \\ M_G = \frac{1.5 n_p \phi_f i_q}{\eta_1} = \frac{k_1}{\eta_1} i_q \end{cases} \quad (3)$$

where u_q is the q -axis voltage, L_q is the q -axis inductance, R_s is the stator winding resistance, u_{q0} is the q -axis voltage without the feedforward decoupling, M_G is the PMSG moment, η_1 is the PMSG mechanical efficiency, and $k_1 = 1.5 n_p \phi_f$ is the proportional coefficient between M_G and i_q .

The speed-increase mechanism is described as:

$$M_{PTO} = \frac{k_2}{\eta_2} M_G \quad (4)$$

where η_2 is the mechanical efficiency.

The inverse pendulum dynamic model is written as:

$$(J_{P+M} + J_{55\infty}) \ddot{\theta}(t) + \int_0^t K(t-\tau) \dot{\theta}(\tau) d\tau + (F_B l_B - G_P l_P - G_M (l_{M0} + X)) \sin \theta(t) = M_E + M_{PTO} + M_{end} \quad (5)$$

where J_{P+M} is the total moment of inertia, $J_{55\infty}$ is the added mass at infinite frequency, θ is the swing angle, $K(t)$ is the impulse response function derived from the radiation damping and added mass, F_B is the buoyancy force, G_P is the pendulum hull gravity force, G_M is the internal mass gravity force, l_B/l_P is the distance between the buoyancy center/pendulum hull mass center and the rotation center, l_{M0} is the distance between the lower limit of the internal mass position and the rotation center, X is the adjustable internal mass position, and M_{end} is the endstop moment to prevent θ from exceeding its limits. Detailed formulas of M_E and M_{end} can be found in Ref. [32].

Herein, J_{P+M} is the function of X and can be expressed as:

$$J_{P+M} = J_P + J_{M0} + m_M(l_{M0} + X)^2 \quad (6)$$

where J_P is the pendulum hull moment of inertia against the rotation center, J_{M0} is the internal mass moment of inertia against the mass center of the internal mass, and m_M is the mass of the internal mass.

Power/efficiency at each link of power generation can be calculated as follows:

$$\begin{cases} \bar{P}_{IN} = Jb_{NIPWEC} \\ P_{PTO} = -M_{PTO}\dot{\theta} \\ P_M = -M_G\omega_G \\ P_G = -1.5u_qi_q \\ \bar{P}_{L_WEC} = \bar{P}_{IN} - \bar{P}_{PTO} \\ \bar{P}_{L_PTO} = \bar{P}_{PTO} - \bar{P}_G \\ CWR = \bar{P}_{PTO}/\bar{P}_{IN} \\ \eta_{PTO} = \bar{P}_G/\bar{P}_{PTO} \end{cases} \quad (7)$$

where P_{IN} , P_{PTO} , P_M , and P_G are the input wave power, the absorbed power by the PTO, the output power from the speed-increase mechanism, and the output electric power from the PMSG, respectively, J is the wave power level, b_{NIPWEC} is the NIPWEC width, P_{L_WEC} is the power loss from ocean waves to the PTO, P_{L_PTO} is the power loss in the PTO, CWR is the capture width ratio, and η_{PTO} is the PTO efficiency. In addition, a symbol with “—” means a time-averaged value.

Energy at each link of power generation can be computed as follows:

$$E_* = \int_0^t P_* dt \quad (8)$$

where E_*/P_* is the total energy/instantaneous power passing through a certain link “*”, t is the current instant, and dt is the time differential. For example, E_{PTO}/P_{PTO} indicates the absorbed energy/power of a PTO.

2.3.2. Mathematical Models of the PMSM Servo Control for LTB IPA

The PMSM servo controller was designed on the basis of the PMSM vector control, whose structure is similar to that of the aforementioned PMSG vector control. Additionally, this PMSM servo controller contains three regulators from the outside to the inside. Firstly, the outermost layer is a position loop proportional (P) regulator which generates a velocity control signal, i.e., the reference internal mass velocity v_m^* , according to the error between X^* and the measured X . According to Ref. [8], proportional control is enough for position tracking. Secondly, the middle layer is a velocity loop PI regulator which produces a current control signal, i.e., the reference PMSM q -axis current i_{qm}^* , based on the error between v_m^* and the measured internal mass velocity v_m . Thirdly, the innermost layer is the current loop PI regulator based on the 0 d -axis current control. This current loop PI regulator as well as the SVPWM-based three-phase inverter can also be simplified by the SM proposed in Section 2.3.1, in order to reduce the computational burden.

Therefore, PMSM servo control for LTB IPA can be simplified as per the block diagram illustrated by Figure 6. Mathematical models of key links are displayed below.

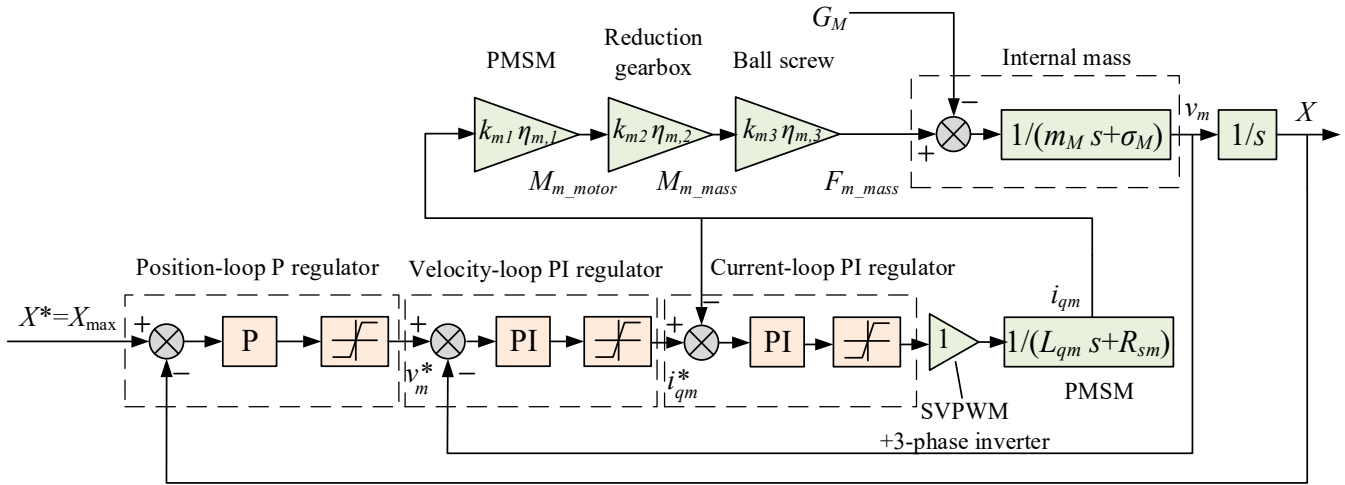


Figure 6. Block diagram of the PMSM servo control for LTB IPA.

The position loop P regulator is expressed as follows:

$$v_m^* = \begin{cases} (K_{X_p})(X^* - X), & |v_m^*| \leq v_{m\max}^* \\ \text{sgn}(v_m^*)v_{m\max}^*, & |v_m^*| > v_{m\max}^* \end{cases} \quad (9)$$

where K_{X_p} is the proportional coefficient, and $v_{m\max}^*$ is the upper bound of v_m^* .

The velocity loop PI regulator is described as:

$$i_{qm}^* = \begin{cases} \left(K_{vm_p} + \frac{K_{vm_i}}{s} \right) (v_m^* - v_m), & |i_{qm}^*| \leq i_{qm\max}^* \\ \text{sgn}(i_{qm}^*)i_{qm\max}^*, & |i_{qm}^*| > i_{qm\max}^* \end{cases} \quad (10)$$

where K_{vm_p}/K_{vm_i} is the proportional/integral coefficient, and $i_{qm\max}^*$ is the upper bound of i_{qm}^* .

The PMSM current loop PI regulator model is expressed as follows:

$$u_{qm0}^* = \begin{cases} \left(K_{qm_p} + \frac{K_{qm_i}}{s} \right) (i_{qm}^* - i_{qm}), & |u_{qm0}^*| \leq u_{qm0\max}^* \\ \text{sgn}(u_{qm0}^*)u_{qm0\max}^*, & |u_{qm0}^*| > u_{qm0\max}^* \end{cases} \quad (11)$$

where u_{qm0}^* is the reference q -axis voltage without the feedforward decoupling, K_{qm_p}/K_{qm_i} is the proportional/integral coefficient, i_{qm} is the PMSM q -axis current, and $u_{qm0\max}^*$ is the upper bound of u_{qm0}^* .

The PMSM model is expressed as follows:

$$\begin{cases} i_{qm} = \frac{u_{qm} - \phi_{fm}n_{pm}\omega_m}{L_{qm}s + R_{sm}} = \frac{u_{qm0}}{L_{qm}s + R_{sm}} \\ M_{m_motor} = 1.5n_{pm}\phi_{fm}i_{qm}\eta_{m,1} = k_{m1}\eta_{m,1}i_{qm} \end{cases} \quad (12)$$

where u_{qm} is the q -axis voltage, ϕ_{fm} is the rotor flux, n_{pm} is the pole-pair number, ω_m is the PMSM angular velocity, L_{qm} is the q -axis inductance, R_{sm} is the stator winding resistance, u_{qm0} is the q -axis voltage without the feedforward decoupling, M_{m_motor} is the PMSM moment, $\eta_{m,1}$ is the PMSM mechanical efficiency, and $k_{m1} = 1.5n_{pm}\phi_{fm}$ is the proportional coefficient between M_{m_motor} and i_{qm} .

The reduction gearbox can be denoted as:

$$M_{m_mass} = k_{m2}\eta_{m,2}M_{m_motor} \quad (13)$$

where M_{m_mass} is the reduction gearbox output moment, k_{m2} is the reduction ratio, and $\eta_{m,2}$ is the reduction gearbox mechanical efficiency.

The ball screw model can be expressed as:

$$F_{m_mass} = \frac{2\pi}{L} M_{m_mass} \eta_{m,3} = k_{m3} \eta_{m,3} M_{m_mass} \tag{14}$$

where F_{m_mass} is the MPAM force, L is the screw lead, $\eta_{m,3}$ is the ball screw efficiency, and $k_{m3} = 2\pi/L$ is the proportional coefficient between F_{m_mass} and M_{m_mass} .

The internal mass is represented as:

$$v_m = \frac{F_{m_mass} - G_M}{m_{MS} + \sigma_M} \tag{15}$$

where σ_M is the equivalent viscous friction coefficient.

Herein, the PMSM servo control is designed for the bidirectional energy transfer for the sake of energy conservation and cost-effectiveness improvement of the internal mass position adjustment. This means that, if the internal mass is upraised, the PMSM will work at a motor mode and consume electricity. Meanwhile, if the internal mass is downgraded, the PMSM will operate at a generator mode and absorb the potential energy from the internal mass. Hence, the efficiency of each link, i.e., $\eta_{m,1}$, $\eta_{m,2}$, and $\eta_{m,3}$, should be updated for the bidirectional energy transfer:

$$\eta_{m,i} = \sigma(k_\sigma v_m) \eta_{m0,i} + \sigma(-k_\sigma v_m) (1/\eta_{m0,i}), \quad i = 1, 2, 3 \tag{16}$$

wherein σ is the sigmoid function used for the smooth efficiency transition between the positive velocity and the negative one, k_σ is the coefficient reflecting the σ steepness around zero velocity, $\eta_{m0,i}$ is the constant efficiency value for the i -th link. Herein, we utilize σ instead of the symbolic function in order to avoid discontinuity at zero velocity and improve the computational efficiency. A similar method has also been proposed by Hansen et al. [35].

Power/efficiency at each link of the MPAM can be calculated as follows:

$$\begin{cases} P_{me} = 1.5u_{qm}i_{qm} \\ P_{mmotor} = M_{m_motor}\omega_m \\ P_{mg} = M_{m_mass}\omega_m \\ P_{ms} = F_{m_mass}v_m \\ P_{mmass} = G_M v_m \\ \bar{P}_{L_MPAM} = \bar{P}_{me} - \bar{P}_{mmass} \\ \eta_{MPAM} = \bar{P}_{mmass} / \bar{P}_{me} \end{cases} \tag{17}$$

where P_{me} , P_{mmotor} , P_{mg} , P_{ms} , and P_{mmass} are the input electric power into PMSM, the output power from the PMSM, the output power from the reduction gearbox, the output power from the ball screw, and the consumption power overcoming the internal mass gravity, respectively, \bar{P}_{L_MPAM} is the power loss in the MPAM, and η_{MPAM} is the MPAM efficiency.

Energy at each link of the MPAM can also be expressed as in Equation (8).

3. Parameter Configuration and Simulation Settings

3.1. Parameters of the MLTB MPPT for a NIPWEC

Design parameters of the NIPWEC and the MLTB MPPT-based wave power controller are listed in Tables 1 and 2. This paper adopts the same geometrical/inertial/hydrodynamic parameters of a NIPWEC as Ref. [32]. In addition, the 1-D resonance position table and 2-D optimal PTO damping table are also identical to those in Ref. [32].

Table 1. NIPWEC design parameters.

Component	Parameter	Value	Unit
Inverse pendulum	J_P	5.138×10^4	[kg·m ²]
	J_{M0}	1.025×10^5	[kg·m ²]
	m_M	9.306×10^4	[kg]
	l_{M0}	0.2	[m]
	$J_{55\infty}$	1.844×10^5	[kg·m ²]
	F_B	1.014×10^6	[N]
	l_B	1.726	[m]
	G_P	1.015×10^5	[N]
	l_P	1.12	[m]
MPAM	G_M	9.129×10^5	[N]
	n_{pm}	6	[-]
	Φ_{fm}	0.2	[Wb]
	L_{qm}	0.0015	[H]
	R_{sm}	0.1	[Ω]
	$\eta_{m0,1}$	0.98	[-]
	k_{m2}	100	[-]
	$\eta_{m0,2}$	0.95	[-]
	L	0.02	[m]
	$\eta_{m0,3}$	0.92	[-]
Speed-increase mechanism	σ_M	1100	[Nm ⁻¹ s]
	k_2	120	[-]
PMSG	η_2	0.95	[-]
	n_p	3	[-]
	ϕ_f	0.6	[Wb]
	L_q	0.0018	[H]
	R_s	0.05	[Ω]
	η_1	0.98	[-]

Table 2. Design parameters for the wave power controller.

Component	Parameter	Value	Unit
MLTB MPPT processor	R_{PTOmax}	2-D optimal PTO damping table	[Nms]
	X_{max}	1-D resonance position table	[m]
PMSG vector controller	K_{q-p}	31.4	[Ω]
	K_{q-i}	872.7	[Ω s ⁻¹]
	u_{q0max}^*	1039	V
PMSM servo controller	K_{X-p}	1	[s ⁻¹]
	v_{mmax}^*	0.005	[m/s]
	K_{vm-p}	500	[Am ⁻¹ s]
	K_{vm-i}	3×10^4	[Am ⁻¹]
	i_{qmmax}^*	48.4	[A]
	K_{qm-p}	5	[Ω]
	K_{qm-i}	200	[Ω s ⁻¹]
	u_{qm0max}^*	207.8	[V]

3.2. Parameters of the Irregular Wave Environments

Parameters of the investigated eight irregular sea states (SSs) are listed in Table 3. Herein, the researched significant wave heights H_s and energy periods T_e of all SSs are common at the P6 position in the offshore area of the East China Sea [36]. The wave spectra of the eight SSs are illustrated in Figure 7.

This paper researched the performance of the MLTB MPPT in two changing sea state processes. The first one, i.e., Process 1, is the process of SS1–SS5–SS3–SS4, while the second one, i.e., Process 2, refers to the process of SS7–SS2–SS8–SS6. Process 1 involves the switches

between standard JONSWAP spectra with the different significant wave heights and peak periods, while Process 2 refers to the transitions between different wave spectrum types. Additionally, the duration of each sea state is set to 1500 s. Therefore, each process has a simulation duration of 6000 s.

Table 3. Parameter settings for the simulated sea states. Herein, $H_{s,i}$, $T_{p,i}$, and λ_i ($i = 1, 2$) indicate the significant wave height, peak period, and shape parameter of the low/high frequency section for an Ochi–Hubble spectrum, respectively. T_p represents the peak period. γ refers to the peak enhancement factor, which is positively correlated with the slenderness of a spectrum peak.

Sea State	Wave-Spectrum Type	H_s or $H_{s,1}/H_{s,2}$ (m)	T_p or $T_{p,1}/T_{p,2}$ (s)	λ_1/λ_2	T_e (s)
SS1	Standard JONSWAP spectrum ($\gamma = 3.3$)	1.5	4	/	3.61
SS2	Standard JONSWAP spectrum ($\gamma = 3.3$)	1.5	6	/	5.42
SS3	Standard JONSWAP spectrum ($\gamma = 3.3$)	1.5	9	/	8.13
SS4	Standard JONSWAP spectrum ($\gamma = 3.3$)	0.5	6	/	5.42
SS5	Standard JONSWAP spectrum ($\gamma = 3.3$)	2.5	6	/	5.42
SS6	JONSWAP spectrum ($\gamma = 6$)	1.5	6	/	5.56
SS7	JONSWAP spectrum ($\gamma = 1$), i.e., P-M spectrum	1.5	6	/	5.14
SS8	Ochi-Hubble spectrum	1.5 or 1.12/1.03	8.36 or 8.36/4.76	3.43/2.04	6.35

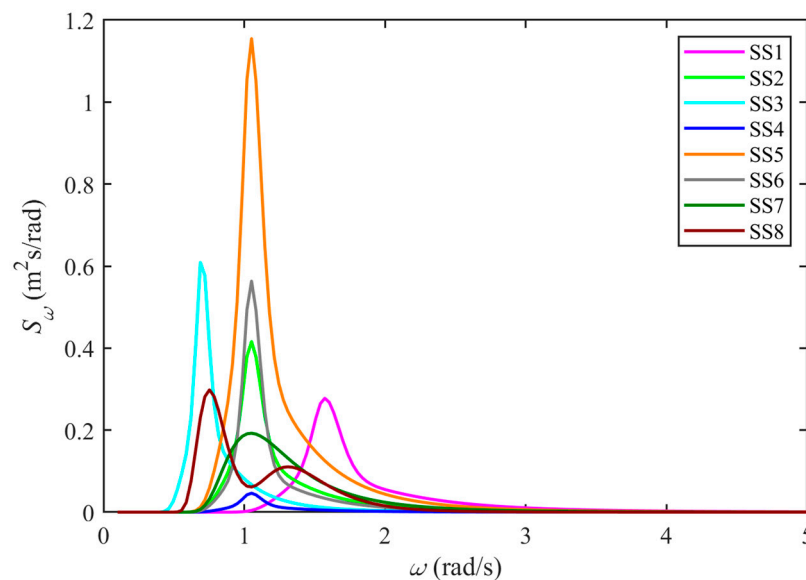


Figure 7. Wave spectra of the eight sea states.

3.3. Other Simulation Settings

Investigation into the MLTB MPPT for a NIPWEC was conducted as per the description below.

Firstly, the feasibility of the PMSG vector control and the PMSM servo control was validated via the time-domain simulations under the regular wave with a wave period of 6 s and a 0.5 m wave height. For the validation of the PMSG vector control for PTO damping tuning, the PTO damping R_{PTO} was set to 1×10^5 Nms before 150 s and then tuned to 4.9×10^5 Nms at 150 s (simulation duration: 300 s). Meanwhile, the internal mass position X was set to 1 m to ensure resonance. In terms of the PMSM servo control for internal mass adjustment, X was altered from 0 m to 1 m, i.e., the resonance position, after 300 s, and then altered from 1 m to 0 m after 700 s (simulation duration: 1000 s). Meanwhile, the R_{PTO} was fixed at 4.9×10^5 Nms.

Secondly, FFT performance in the energy period estimation was assessed separately. Herein, FFT sampling frequency was set to 10 Hz. The historical WESs within the past durations of 100–600 s (with an interval of 100 s) were adopted for FFT in order to evaluate

the influence of the historical WES length on the FFT performance. Additionally, a Savitzky–Golay (S–G) filter [37] was utilized to smooth the wave spectrum obtained via the FFT.

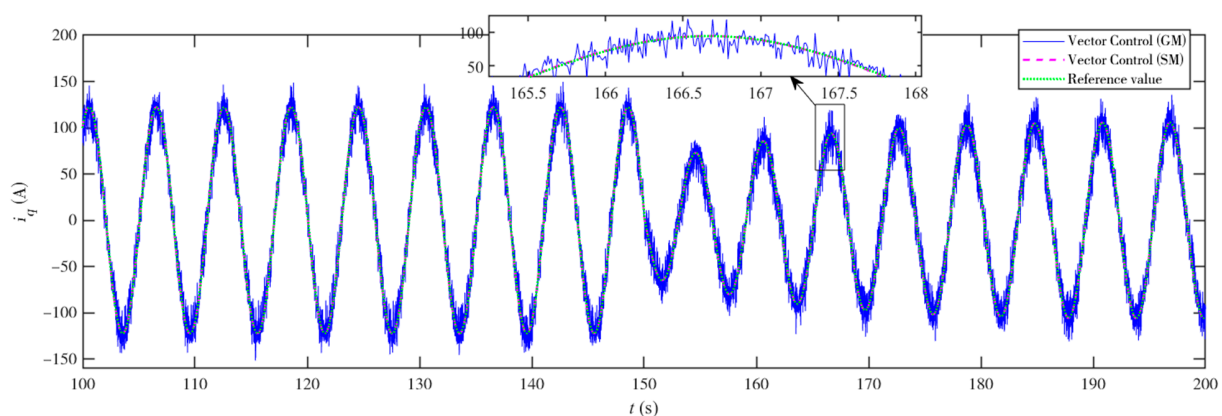
Thirdly, MLTB MPPT performance in the absorbed-power enhancement was further researched via the time-domain simulations under variable irregular waves. Herein, we considered the cases of $n_w = 1–10$ for the LTB PTO damping tuning. Additionally, two obtainment methods, i.e., Method 1 and Method 2, for H_{n_w} and T_{n_w} were also studied.

Furthermore, two other MPPT algorithms were introduced for comparison. The first one was the FACB MPPT, while the second one was the LTB IPA combined with the optimal fixed damping search (LTB IPA+OFDS). Herein, the FACB MPPT references a similar one proposed by Ref. [14]. It contains two parts. The first part is the frequency control, i.e., tuning mass position according to the peak period T_P for the wave spectrum of a historical WES. Meanwhile, the second part consists of the amplitude control, i.e., tuning PTO damping to be identical to the inherent impedance amplitude, which can be accurately calculated using a specific formula [14]. Additionally, LTB IPA+OFDS also consists of two parts, i.e., the LTB IPA, which is fully consistent with that of the MLTB MPPT, and the ergodic search for the optimal fixed damping of a certain sea state via massive irregular-wave time-domain simulations based on a historical WES. Compared to two other algorithms, LTB IPA+OFDS is more complex and time-consuming, and brings up the higher hardware requirements. Moreover, its performance is strongly correlated with the fidelity of an embedded dynamic model. Here, we made two ideal assumptions to simplify the LTB IPA+OFDS simulations. Firstly, the embedded dynamic model is the same as the real one. Secondly, the search process can be completed within a negligible time period after the processor receives a historical WES.

4. Results and Discussion

4.1. PMSG Vector Control

Simulation results from the PMSG vector control are displayed in Figure 8. Moreover, the comparison between the GM and SM is also shown in this figure. Herein, GM has the same current loop PI regulator parameters as SM. The results reveal that both the GM and SM of the PMSG vector control can effectively emulate the theoretical value changes in M_{PTO} or P_{PTO} (see Figure 8b,c). Therefore, the PMSG vector control is able to achieve the PTO damping adjustment. Additionally, the i_q tracking process is well reflected by both the GM and SM (see Figure 8a). Hence, the SM possesses the same control process simulation capability as the GM. In addition, compared with the GM, the SM needs much shorter computational time. Furthermore, the instantaneous power at each link of power generation is unveiled in Figure 8d. Results demonstrate that the SM can also reasonably describe the power losses from the absorbed wave energy to electricity. The simulated PTO efficiency η_{PTO} was 0.89.



(a)

Figure 8. Cont.

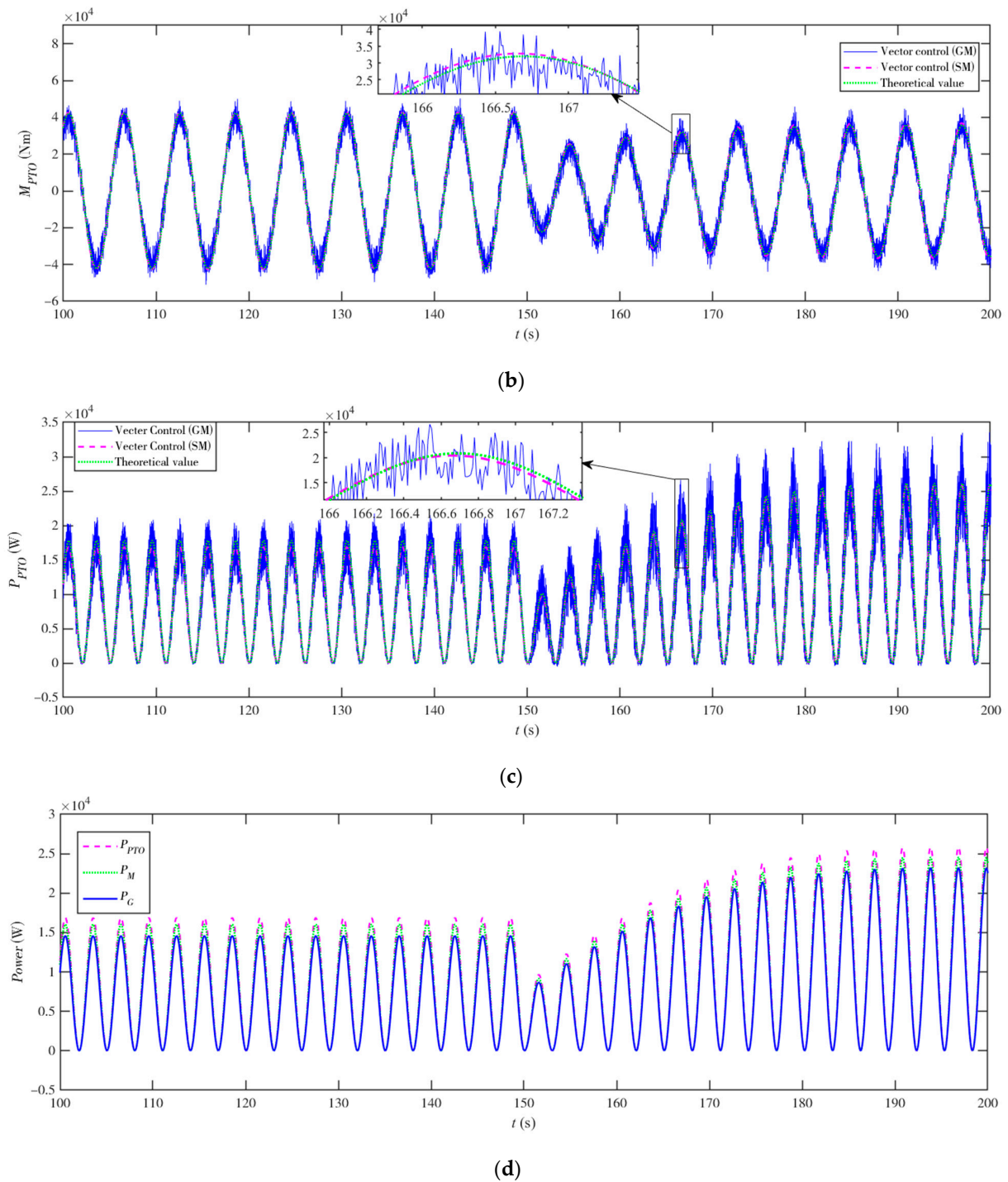
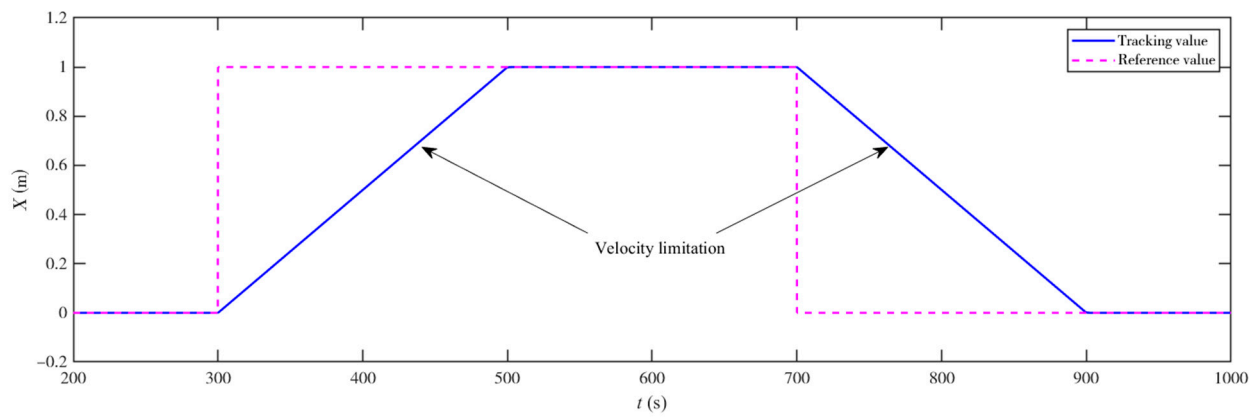


Figure 8. Time-domain response curves under the generator vector control. (a) PMSG q -axis current i_q . (b) PTO moment M_{PTO} . (c) Absorbed power P_{PTO} . (d) Power at each link of power generation (SM). Computational time: 3691.5 s (GM), 4.3 s (SM). Here, both GM and SM were computed by ode23tb.

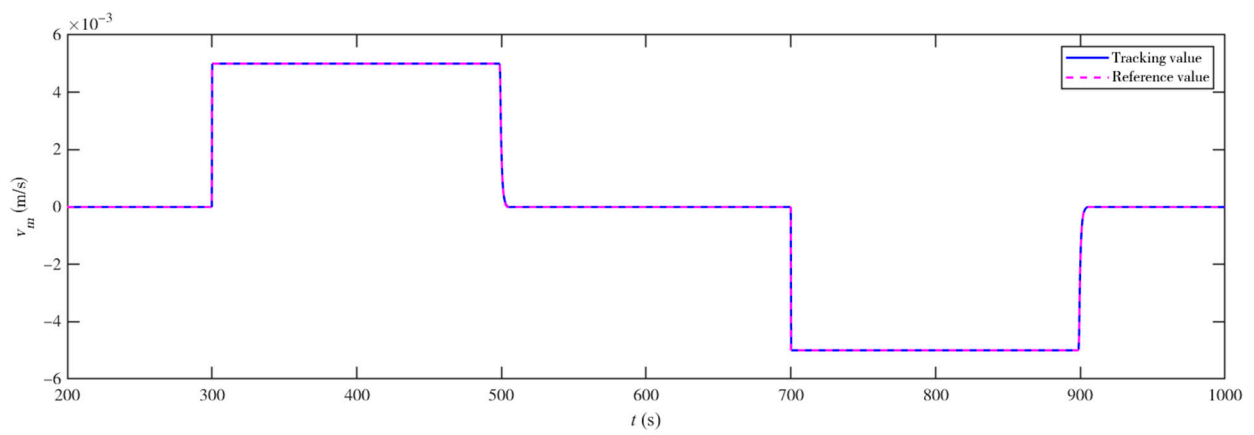
In order to improve computational efficiency, all of the following simulations were based on the SM.

4.2. PMSM Servo Control

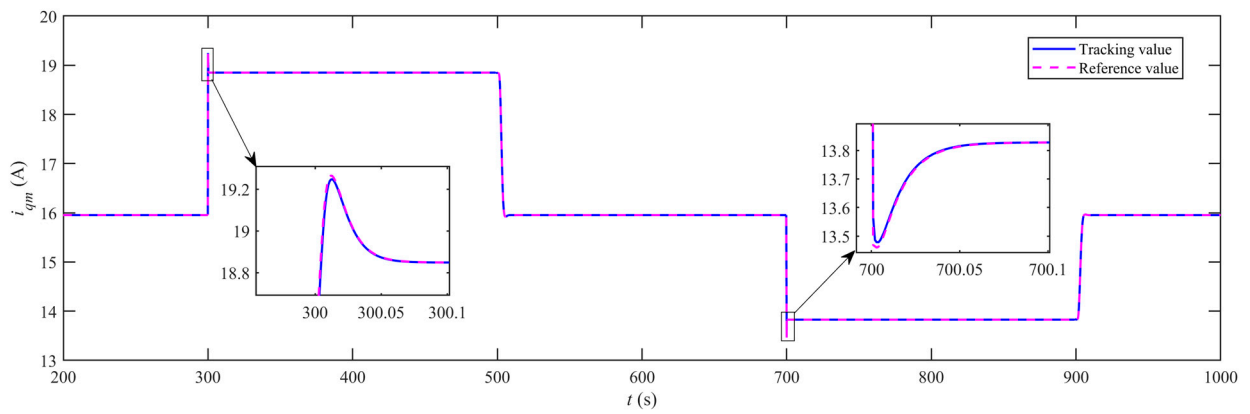
Simulation results of the PMSM servo control are displayed in Figure 9. The results reveal that X , as well as v_m and i_{qm} , can be well tracked via the PMSM servo control. Moreover, the X tracking process is sluggish due to the velocity limitation of 0.005 m/s.



(a)



(b)



(c)

Figure 9. Cont.

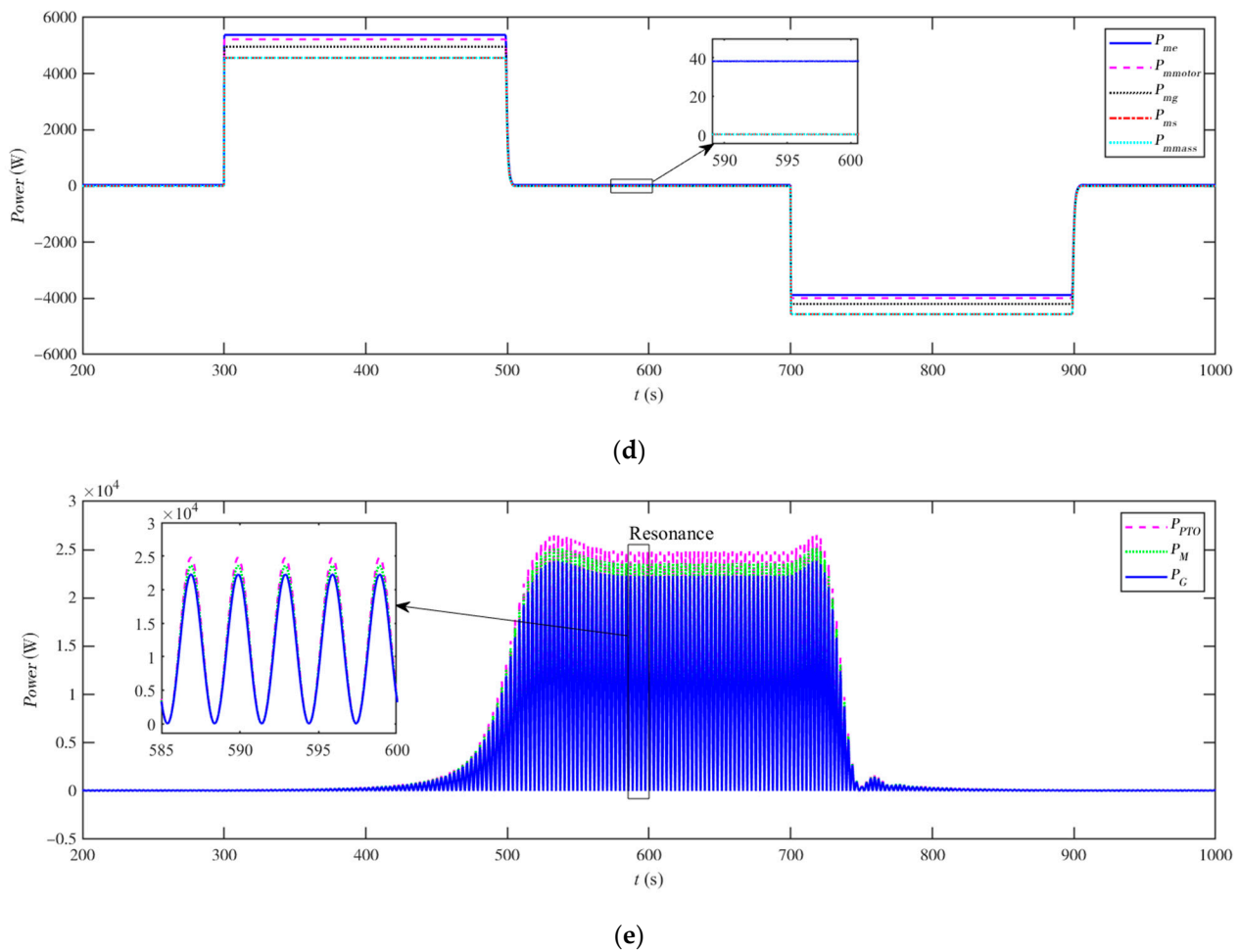


Figure 9. Time-domain response curves under the motor servo control. (a) Internal mass position X . (b) Internal mass velocity v_m . (c) PMSM q -axis current i_{qm} . (d) Power at each link of the internal mass position adjustment. (e) Power at each link of power generation.

Power at each link of the internal mass position adjustment and the power generation is also displayed in Figure 9. In terms of internal mass position adjustment, the results indicate that the PMSM operates in motor mode when X rises. In this mode, the output power from the PMSM to the internal mass is positive and has a monotonically decreasing trend. Furthermore, PMSM operates in generator mode when X declines. In this mode, the output power from the PMSM to the internal mass is negative and has a monotonically increasing trend in terms of the absolute value. The overall efficiency of the aforementioned two modes is about 0.85. In addition, if the X is fixed at a constant value, such as 1 m, there will still exist the P_{me} of 38.2 W to maintain M_{m_motor} . This phenomenon is consistent with reality. With respect to power generation, results well describe the power losses from the absorbed wave energy to electricity and the effective P_{PTO}/P_C enhancement caused by resonance.

4.3. MLTB MPPT under Variable Irregular Waves

4.3.1. Simulated Irregular Wave Environments

Variations of the wave elevation and M_E for the two changing sea state processes are shown in Figure 10. Results indicate that M_E exceeds the wave elevation by about $\pi/2$. The amplitude of M_E can reach up to 3.5×10^5 Nm (see SS5 in Figure 10a). In order to assess simulation reliability, the zero-crossing periods T_z and H_s , which are calculated using the statistical analysis for the simulated wave elevation, were compared with the theoretical values directly derived from wave spectra (see Table 4). Results reveal that

simulated T_z and H_s are all close to theoretical values. The maximum absolute value of the relative error for T_z/H_s is lower than 5%. Therefore, the simulated irregular wave environments are reliable.

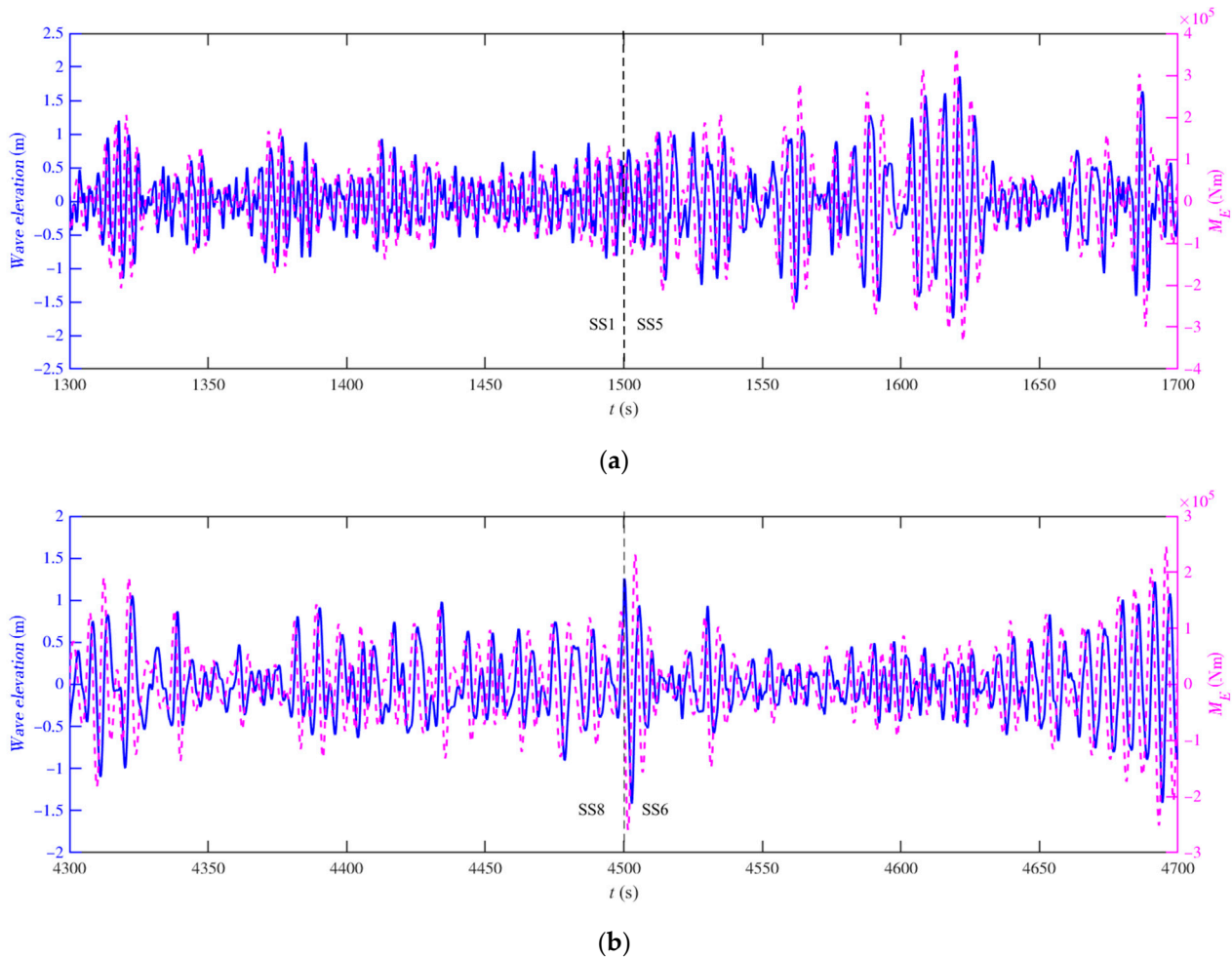


Figure 10. Variations of the wave elevation and M_E for two changing sea state processes. (a) Process 1. (b) Process 2.

Table 4. Reliability study of the simulated irregular wave environments. Herein, T_z is the zero-crossing period. Theoretical value indicates the value computed based on the wave spectrum. Simulated value represents the value calculated using the statistical analysis for the simulated wave elevation. Moreover, $|\delta_{T_z}|/|\delta_{H_s}|$ is the absolute value of the relative error between the simulated T_z/H_s and its theoretical value.

Sea State	T_z (s)			H_s (m)		
	Theoretical Value	Simulated Value	$ \delta_{T_z} $	Theoretical Value	Simulated Value	$ \delta_{H_s} $
SS1	3.15	3.25	3.3%	1.50	1.45	3.4%
SS2	4.69	4.52	3.5%	1.50	1.46	2.5%
SS3	7.01	7.17	2.3%	1.50	1.47	2.1%
SS4	4.69	4.60	1.9%	0.50	0.48	4.7%
SS5	4.69	4.52	3.5%	2.50	2.44	2.5%
SS6	4.93	4.81	2.4%	1.50	1.44	4.1%
SS7	4.29	4.39	2.4%	1.50	1.43	4.4%
SS8	5.29	5.17	2.4%	1.50	1.44	4.1%

4.3.2. Performance Analysis for the FFT

The estimated energy periods against different historical WES durations are listed in Table 5. It can be seen that applying an FFT to the WES of 200 s is enough for the accuracy requirement. Because the maximum absolute value of the relative error $|\delta_{T_e}|$ between the estimated energy period $\widehat{T_e}$ and T_e is only 1.5%, this is tolerable for the energy period estimation. Additionally, the average $|\delta_{T_e}|$ is 0.5%, which corresponds to the magnitude of the 400–600 s FFT.

Table 5. Estimated energy periods $\widehat{T_e}$ against different historical WES durations (FFT). Herein, $\widehat{T_e}$ at each cell indicates the mean value of three estimated results, while $|\delta_{T_e}|$ indicates the absolute value of the relative error between $\widehat{T_e}$ and T_e . The maximum $|\delta_{T_e}|$ of each historical WES duration is shown in bold and underlined.

Sea State	T_e (s)	$\widehat{T_e}$ (s) (FFT)											
		100 s	$ \delta_{T_e} $	200 s	$ \delta_{T_e} $	300 s	$ \delta_{T_e} $	400 s	$ \delta_{T_e} $	500 s	$ \delta_{T_e} $	600 s	$ \delta_{T_e} $
SS1	3.61	3.71	2.8%	3.64	0.9%	3.65	1.0%	3.64	0.8%	3.64	0.8%	3.64	0.8%
SS2	5.42	5.57	2.9%	5.43	0.2%	5.49	1.4%	5.43	0.2%	5.46	0.7%	5.45	0.6%
SS3	8.13	8.31	2.3%	8.25	<u>1.5%</u>	8.27	1.7%	8.20	<u>0.9%</u>	8.21	0.9%	8.20	<u>0.9%</u>
SS4	5.42	5.57	2.9%	5.43	0.2%	5.49	1.4%	5.43	0.2%	5.46	0.7%	5.45	0.6%
SS5	5.42	5.57	2.9%	5.43	0.2%	5.49	1.4%	5.43	0.2%	5.46	0.7%	5.45	0.6%
SS6	5.56	5.68	2.2%	5.57	0.1%	5.62	1.1%	5.56	0.1%	5.59	0.6%	5.58	0.4%
SS7	5.14	5.35	<u>4.1%</u>	5.16	0.5%	5.23	1.8%	5.17	0.5%	5.19	1.0%	5.18	0.8%
SS8	6.35	6.56	3.4%	6.39	0.6%	6.49	<u>2.2%</u>	6.38	0.4%	6.43	<u>1.2%</u>	6.39	0.7%
Average value			2.9%		0.5%		1.5%		0.4%		0.8%		0.7%

Here, SS8 WES within 0–200 s is taken as an example (see Figure 11), for the sake of visual evaluation of the effectiveness of a FFT with respect to the computation of the wave spectrum. Results show that the wave spectrum density, which was computed using the FFT combined with the five-order S–G filter with a frame length of 15, is largely consistent with the theoretical wave spectrum density of SS8. The coefficient of determination is 0.96.

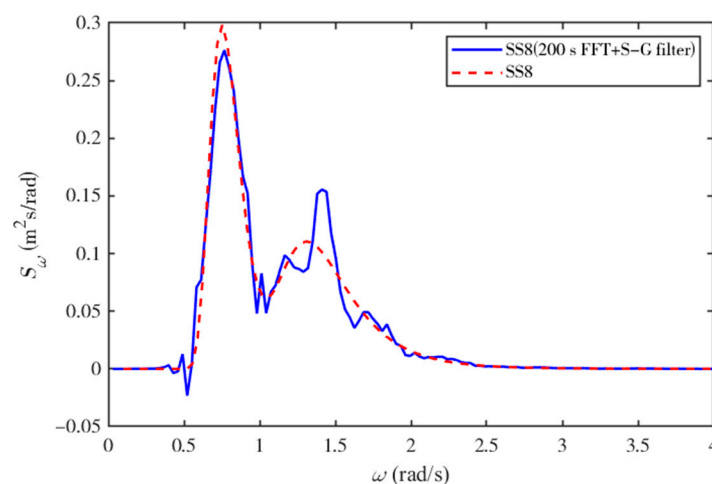


Figure 11. Wave spectrum computation results for the SS8 WES within 0–200 s. Herein, S_w indicates the wave spectrum density, while ω indicates the wave angular frequency. The polynomial order and frame length of an S–G filter are 5 and 15, respectively. Root-mean-square error between the results computed by “200 s FFT+S–G filter” and the theoretical data is 0.01. Meanwhile, the coefficient of determination is 0.96.

In summary, FFT of a 200 s WES is enough for the energy period estimations of the sea states of $T_e \leq 8.13$ s.

4.3.3. Performance Analysis for the MLTB MPPT

Comparison of the three MPPT algorithms in terms of the maximum absorbed power (P_{PTO}) tracking are illustrated by Figure 12. All MPPT algorithms are implemented based on the FFT for the 200 s WES after each sea state variation. For example, LTB IPA of the MLTB MPPT starts at 200 s, 1700 s, 3200 s, and 4700 s to make sure that the FFT of a 200 s WES for each sea state has already been conducted. Moreover, the simulation results against the LTB IPA combined with the prior optimal fixed damping (POFD) are also given.

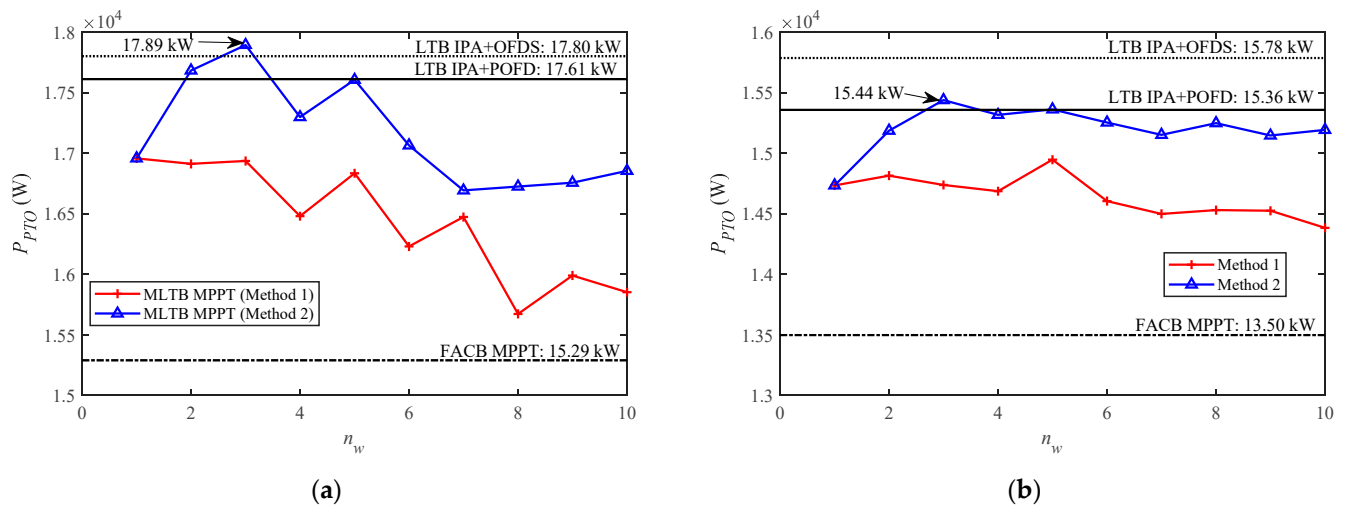


Figure 12. Comparison of three MPPT algorithms in terms of maximum absorbed power (P_{PTO}) tracking. (a) Process 1. (b) Process 2.

Results show that both the MLTB MPPT (Method 2) and the LTB IPA+OFDS can obtain the basically equivalent P_{PTO} to LTB IPA+POFD. However, P_{PTO} of the FACB MPPT can only reach 87–88% of that of the POFD. MLTB MPPT (Method 2) is able to get more P_{PTO} than the LTB IPA+OFDS (see the blue point against $n_w = 3$, Figure 12a). In addition, P_{PTO} values of the MLTB MPPT (Method 1) are all equal to or less than those of the MLTB MPPT (Method 2). This means that the R_{PTOmax} query based on (H_m, T_m) is better than that based on $(H_{m,1/3}, T_{m,1/3})$. Furthermore, both the MLTB MPPT (Method 2) and MLTB MPPT (Method 1) are better than the FACB MPPT.

In other words, MLTB MPPT (Method 2) is a competitive algorithm under variable irregular waves, affording results comparable to those produced by other methods. It has a similar tracking performance to that of the LTB IPA+OFDS, especially for $n_w = 3$. Since LTB IPA+OFDS is based on two ideal assumptions, its performance may be weakened in actual situations. Hence, MLTB MPPT (Method 2) possesses a greater application potential.

Time-domain response curves for Process 1 and Process 2 are presented in Figures 13 and 14, respectively, in order to visually reflect the dynamic process of the MLTB MPPT implementations. Herein, the MLTB MPPT (Method 2) is taken as an example. The $X/R_{PTO}/E_{PTO}$ curves of the FACB MPPT and LTB IPA+OFDS are also displayed. For the sake of evaluation of the superimposition effect of the resonance and optimal PTO damping on the NIPWEC power absorption, the $X/R_{PTO}/E_{PTO}$ curves of the operation without MPPT/of the LTB IPA are introduced. The findings are as follows.

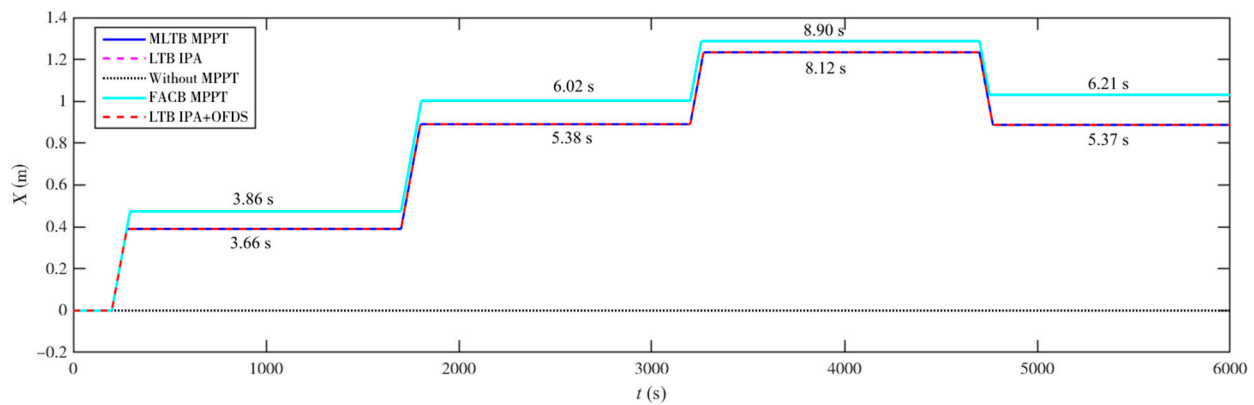
(1) The estimation accuracy of the FFT for the peak period is lower than that for the energy period. For example, the error of a peak period estimation can reach 10% at SS7 (see the light blue curve within 200–1700 s in Figure 13a). This is probably caused by the non-negligible fluctuations in a wave spectrum density curve computed via FFT.

(2) Three MPPT algorithms tunes the PTO damping according to the “optimal” PTO damping, independently discovered by themselves. However, R_{PTO} curves of different MPPT algorithms are quite distinct (see Figures 13b and 14b). In addition, although the MLTB MPPT and LTB IPA+OFDS have a similar tracking performance, it is difficult to

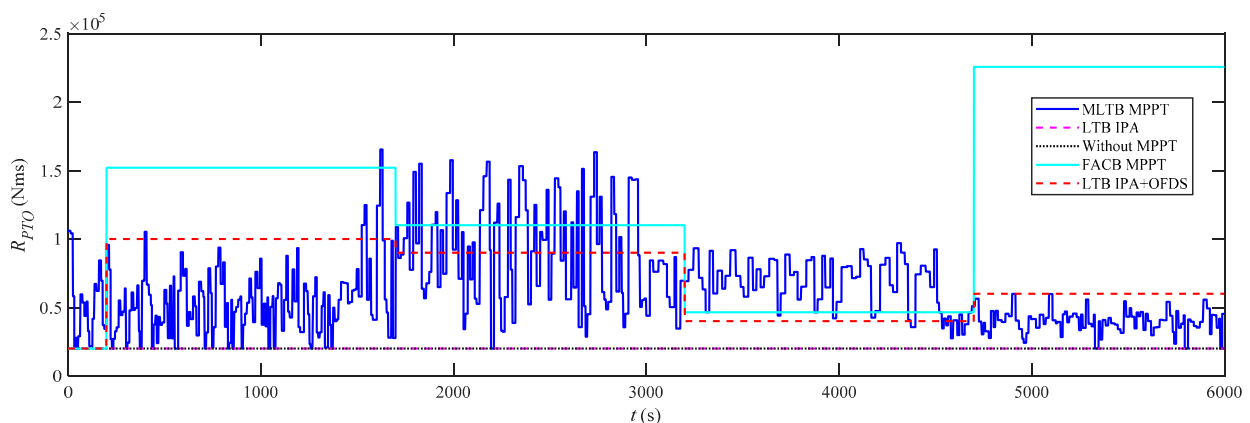
find a correlation between their R_{PTO} curves. Hence, it can be observed that the “optimal” PTO damping of the two MPPT algorithms with the similar tracking performance may be significantly different from one another.

(3) Under the superposition effect of the resonance and the optimal PTO damping, MLTB MPPT can achieve a huge absorbed-power increase which strides over the order of magnitude. Moreover, the E_{PTO} curves of the MLTB MPPT and LTB IPA+OFDS are largely consistent. According to the E_{PTO} curve within 4500–6000 s in Figure 14c, it can be noted that the wave spectrum with a slender peak, e.g., SS6, is able to weaken the MLTB MPPT tracking performance. In addition, the E_{PTO} curve of FACB MPPT lies below the two others most of the time. This means that the FACB MPPT possesses the lowest tracking performance.

(4) A significant portion (>12%) of the time-averaged absorbed power is lost in the power generation, while the power consumed by a MPAM is minuscule. Herein, the time-averaged consumption power of a MPAM is only about 0.2 kW, which is smaller than 1.5% of the time-averaged absorbed power. Furthermore, $\eta_{PTO} = 0.87\sim 0.88$. In consideration of the MPAM consumption, the NIPWEC efficiency from absorbed power to output electric power is about 0.86.

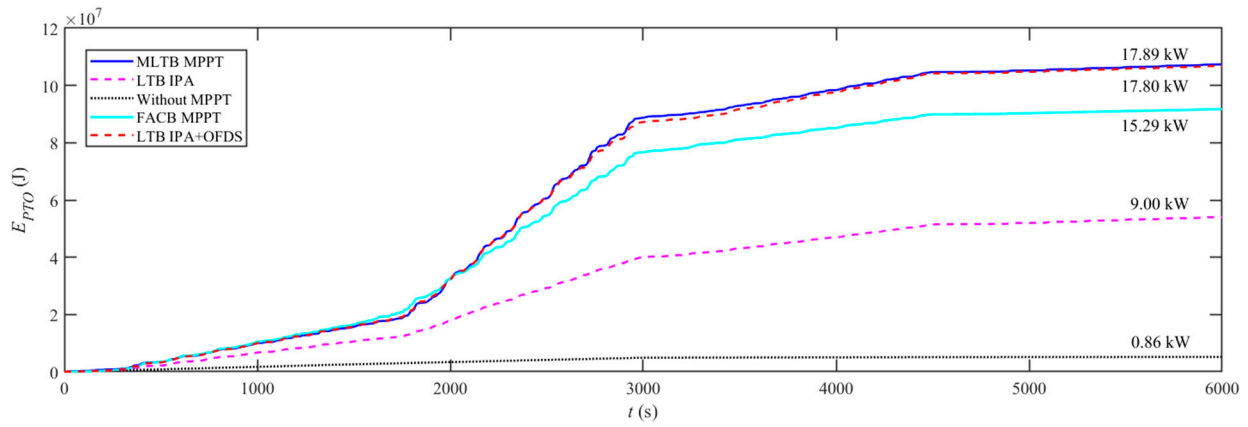


(a)

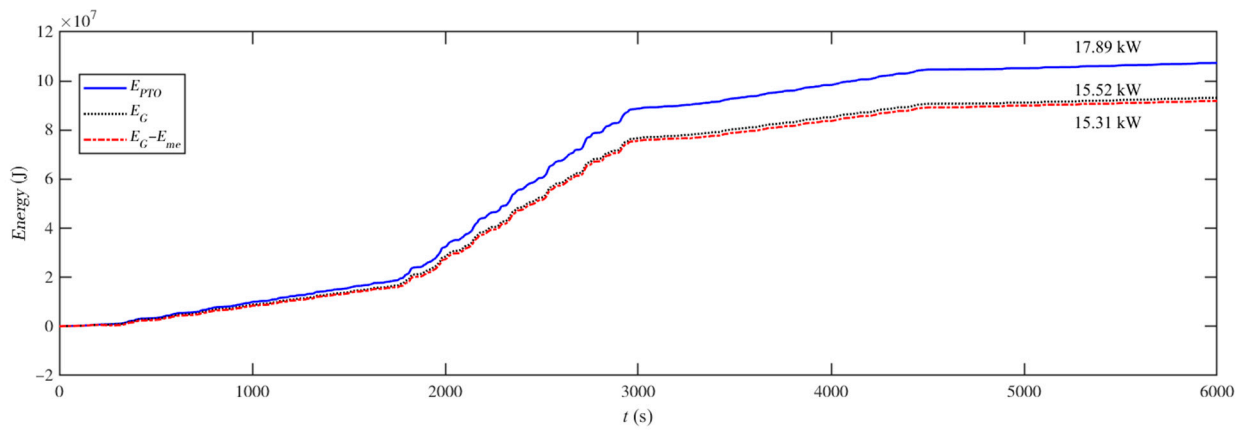


(b)

Figure 13. Cont.

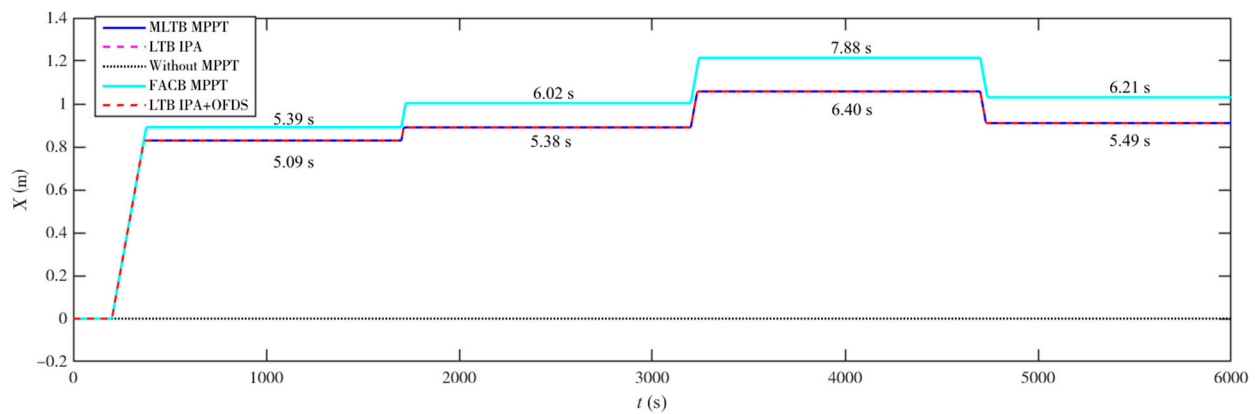


(c)



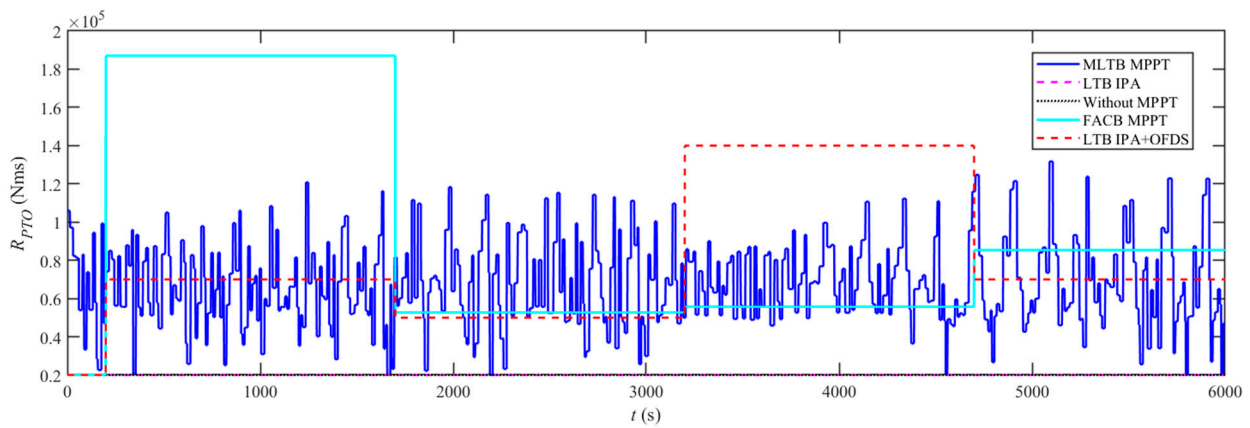
(d)

Figure 13. Time-domain response curves for Process 1 ($n_w = 3$). (a) Internal mass position. (b) PTO damping. (c) Absorbed energy and time-averaged absorbed power. (d) Energy and time-averaged power at each link. In (d), $\bar{P}_{PTO} = 17.89 \text{ kW}$, $\bar{P}_G = 15.52 \text{ kW}$, $\bar{P}_G - \bar{P}_{me} = 15.31 \text{ kW}$.

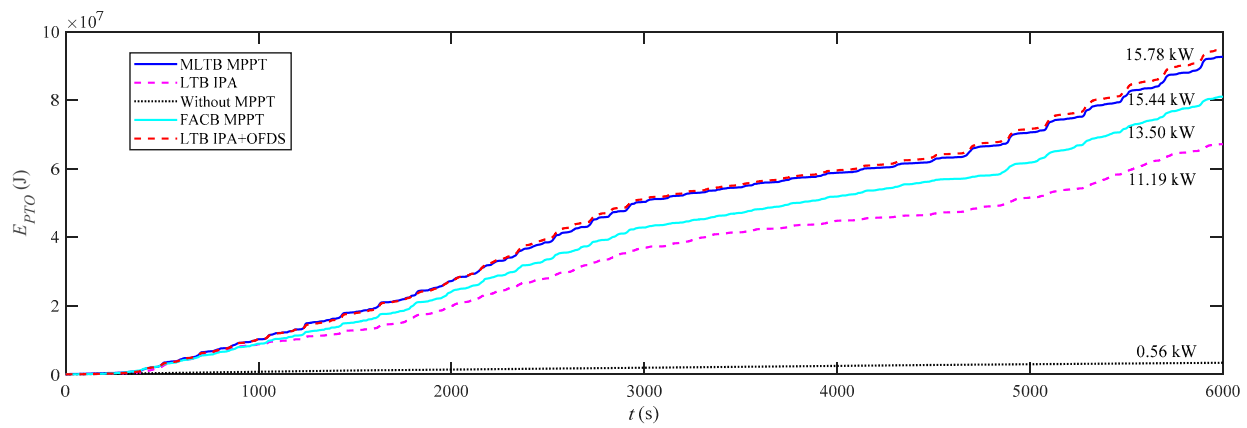


(a)

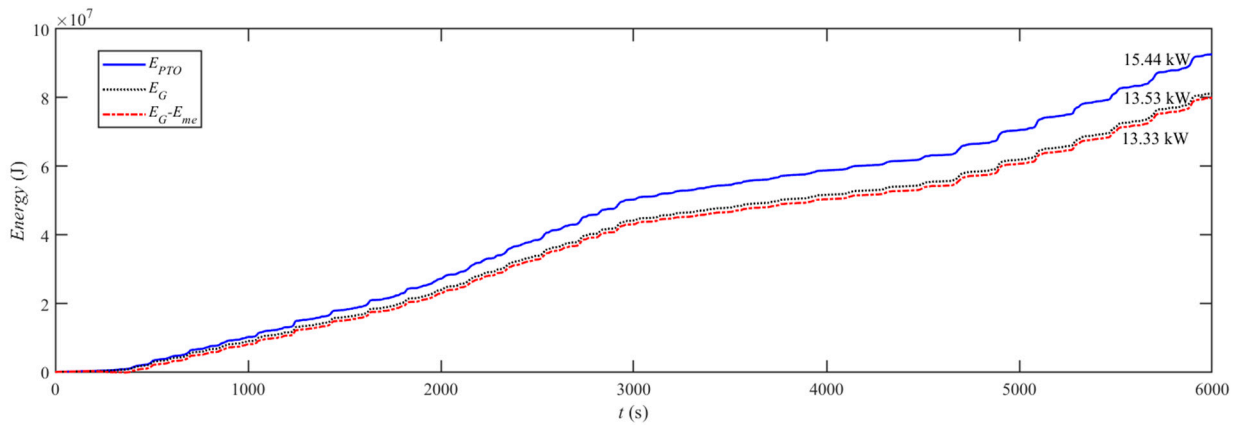
Figure 14. Cont.



(b)



(c)



(d)

Figure 14. Time-domain response curves for Process 2 ($n_w = 3$). (a) Internal mass position. (b) PTO damping. (c) Absorbed energy and time-averaged absorbed power. (d) Energy and time-averaged power at each link. In (d), $\bar{P}_{PTO} = 15.44$ kW, $\bar{P}_G = 13.53$ kW, $\bar{P}_G - \bar{P}_{me} = 13.33$ kW.

5. Conclusions

This paper focuses on the implementation process simulation and performance analysis for the MLTB MPPT under variable irregular waves. First, the overall structure of the NIPWEC and the wave power controller with a MLTB MPPT algorithm was described. Herein, the wave power controller contains three core parts, i.e., a MLTB MPPT processor, a PMSG vector controller, and a PMSM servo controller. Next, the control flow of MLTB MPPT and the mathematical models containing the efficiency of each link were given. Then,

the feasibility of the PMSG vector control/PMSM servo control was validated. Afterwards, the foundation of MLTB MPPT implementations, i.e., FFT, was separately studied in terms of the performance in energy period estimations. Finally, the MLTB MPPT tracking performance under variable irregular waves was comprehensively analyzed via comparison with two other algorithms, i.e., the FACB MPPT and the LTB IPA+OFDS. The main findings are listed below.

(1) The FFT based on a historical wave elevation signal of 200 s can estimate well the energy period T_e ($T_e \leq 8.13$ s) of a certain sea state.

(2) Under the superposition effect of the resonance and the optimal PTO damping, MLTB MPPT can achieve a huge absorbed-power increase which strides over the order of magnitude. In terms of the maximum absorbed power tracking performance, $\text{FACB MPPT} < \text{MLTB MPPT (Method 1)} \leq \text{MLTB MPPT (Method 2)} \approx \text{LTB IPA+OFDS}$. Hence, MLTB MPPT (Method 2) is a competitive algorithm under variable irregular waves.

(3) A significant portion (>12%) of the time-averaged absorbed power is lost in power generation, while the power consumed by a mass-position-adjusting mechanism is small (approximately 0.2 kW, <1.5% of the time-averaged absorbed power), when implementing MLTB MPPT.

Author Contributions: Conceptualization, X.Y.; methodology, X.Y.; software, X.Y. and D.G.; validation, X.Y., F.M. and D.G.; formal analysis, X.Y. and Z.T.; investigation, D.G., F.M. and Z.T.; data curation, J.L.; writing—original draft preparation, X.Y.; writing—review and editing, D.G.; visualization, X.Y.; supervision, Q.C. and J.L.; Resources, F.M. All authors have read and agreed to the published version of the manuscript.

Funding: This research was funded by the National Natural Science Foundation of China (Grant No. 52179088) and the Science & Technology Project of Enterprise (Grant No. ZKY2023-HCDK-02-01).

Data Availability Statement: The data presented in this study are available on request from the corresponding author.

Conflicts of Interest: The authors declare no conflict of interest.

Abbreviations

1-D, 2-D	1-dimensional, 2-dimensional
DC	Direct-current
FACB	Frequency and amplitude control based
FFT	Fast Fourier transformation
GM	General model
IPA	Internal-mass position adjustment
LTB	Lookup table based
MLTB	Multi-timescale lookup table based
MPAM	Mass-position-adjusting mechanism
MPP	Maximum power point
MPPT	Maximum power point tracking
NIPWEC	Novel inverse-pendulum wave energy converter
NPCM	Natural-period control method
OFDS	Optimal fixed damping search
P	Proportional
P&O	Perturbation and observation
PI	Proportional-integral
PMSG	Permanent magnet synchronous generator
PMSM	Permanent magnet synchronous motor
POFD	Prior optimal fixed damping
PTO	Power take-off
PWM	Pulse-width-modulation
S-G	Savitzky–Golay

SM	Simplified model
SS	Sea state
SVPWM	Space vector PWM
WEC	Wave energy converter
WES	Wave elevation signal
WEU	Wave energy utilization

References

- Guo, B.; Ringwood, J.V. A Review of Wave Energy Technology from a Research and Commercial Perspective. *IET Renew. Power Gener.* **2021**, *15*, 3065–3090. [[CrossRef](#)]
- IRENA. *Innovation Outlook: Ocean Energy Technologies*; IRENA: Abu Dhabi, United Arab Emirates, 2020.
- Avalos, G.O.G.; Shadman, M.; Estefen, S.F. Application of the Latching Control System on the Power Performance of a Wave Energy Converter Characterized by Gearbox, Flywheel, and Electrical Generator. *J. Mar. Sci. Appl.* **2021**, *20*, 767–786. [[CrossRef](#)]
- Temiz, I.; Leijon, J.; Ekergård, B.; Boström, C. Economic Aspects of Latching Control for a Wave Energy Converter with a Direct Drive Linear Generator Power Take-Off. *Renew. Energy* **2018**, *128*, 57–67. [[CrossRef](#)]
- Zhang, Y.; Zhan, S.; Li, G. Model Predictive Control of Wave Energy Converters With Prediction Error Tolerance. *IFAC-Pap. Online* **2020**, *53*, 12289–12294. [[CrossRef](#)]
- Zhang, Z.; Qin, J.; Wang, D.; Huang, S.; Liu, Y.; Xue, G. Hybrid Model Predictive Control of a Two-Body Wave Energy Converter with Mechanically Driven Power Take-Off. *J. Mar. Sci. Eng.* **2023**, *11*, 1618. [[CrossRef](#)]
- Budar, K.; Falnes, J. A Resonant Point Absorber of Ocean-Wave Power. *Nature* **1975**, *256*, 478–479. [[CrossRef](#)]
- Costa, P.R.; Garcia-Rosa, P.B.; Estefen, S.F. Phase Control Strategy for a Wave Energy Hyperbaric Converter. *Ocean Eng.* **2010**, *37*, 1483–1490. [[CrossRef](#)]
- Flocard, F.; Finnigan, T.D. Increasing Power Capture of a Wave Energy Device by Inertia Adjustment. *Appl. Ocean Res.* **2012**, *34*, 126–134. [[CrossRef](#)]
- Marei, M.I.; Mokhtar, M.; El-Sattar, A.A. MPPT Strategy Based on Speed Control for AWS-Based Wave Energy Conversion System. *Renew. Energy* **2015**, *83*, 305–317. [[CrossRef](#)]
- Têtu, A.; Ferri, F.; Kramer, M.B.; Todalshaug, J.H. Physical and Mathematical Modeling of a Wave Energy Converter Equipped with a Negative Spring Mechanism for Phase Control. *Energies* **2018**, *11*, 2362. [[CrossRef](#)]
- Temiz, I.; Ekweoba, C.; Thomas, S.; Kramer, M.; Savin, A. Wave Absorber Ballast Optimization Based on the Analytical Model for a Pitching Wave Energy Converter. *Ocean Eng.* **2021**, *240*, 109906. [[CrossRef](#)]
- Wu, J.; Yao, Y.; Li, W.; Zhou, L.; Götteman, M. Optimizing the Performance of Solo Duck Wave Energy Converter in Tide. *Energies* **2017**, *10*, 289. [[CrossRef](#)]
- Dong, F.; Pan, S.; Gong, J.; Cai, Y. Maximum Power Point Tracking Control Strategy Based on Frequency and Amplitude Control for the Wave Energy Conversion System. *Renew. Energy* **2023**, *215*, 118973. [[CrossRef](#)]
- Cai, Y.; Huo, Y.; Shi, X.; Liu, Y. Numerical and Experimental Research on a Resonance-Based Wave Energy Converter. *Energy Convers. Manag.* **2022**, *269*, 116152. [[CrossRef](#)]
- Cai, Y.; Shi, X.; Huo, Y.; Liu, Y. Experimental Study on a Pitching Wave Energy Converter with Adjustable Natural Period. *Ocean Eng.* **2022**, *261*, 112128. [[CrossRef](#)]
- Zheng, Y.; Chen, Q.; Yue, X.; Geng, D.; Niu, Y.; Gu, X. Active-Resonance Technology for Wave Energy Utilization: An Efficient Offshore Distributed Renewable Power Generation Alternative. *Energy Convers. Manag.* **2023**, *292*, 117359. [[CrossRef](#)]
- Amon, E.A. Development of Two-Variable Maximum Power Point Tracking Control for Ocean Wave Energy Converters Utilizing a Power Analysis and Data Acquisition System. Ph.D. Thesis, Oregon State University, Corvallis, OR, USA, 2010.
- Amon, E.A.; Schacher, A.A.; Brekken, T.K.A. A Novel Maximum Power Point Tracking Algorithm for Ocean Wave Energy Devices. In Proceedings of the 2009 IEEE Energy Conversion Congress and Exposition, San Jose, CA, USA, 20–24 September 2009; pp. 2635–2641.
- Amon, E.A.; Brekken, T.K.A.; Schacher, A.A. Maximum Power Point Tracking for Ocean Wave Energy Conversion. *IEEE Trans. Ind. Appl.* **2012**, *48*, 1079–1086. [[CrossRef](#)]
- Zhou, Y. Research on the Power Control Technology of Floating Pendulum Wave Energy Converter. Master's Thesis, Zhejiang University, Hangzhou, China, 2019.
- Yue, X.; Geng, D.; Chen, Q.; Zheng, Y.; Gao, G.; Xu, L. 2-D Lookup Table Based MPPT: Another Choice of Improving the Generating Capacity of a Wave Power System. *Renew. Energy* **2021**, *179*, 625–640. [[CrossRef](#)]
- Zhao, A.; Wu, W.; Sun, Z.; Zhu, L.; Lu, K.; Chung, H.; Blaabjerg, F. A Flower Pollination Method Based Global Maximum Power Point Tracking Strategy for Point-Absorbing Type Wave Energy Converters. *Energy* **2019**, *12*, 1343. [[CrossRef](#)]
- Xu, J.; Yang, Y.; Hu, Y.; Xu, T.; Zhan, Y. MPPT Control of Hydraulic Power Take-off for Wave Energy Converter on Artificial Breakwater. *J. Mar. Sci. Eng.* **2020**, *8*, 304. [[CrossRef](#)]
- Ding, B.; Cazzolato, B.S.; Arjomandi, M.; Hardy, P.; Mills, B. Sea-State Based Maximum Power Point Tracking Damping Control of a Fully Submerged Oscillating Buoy. *Ocean Eng.* **2016**, *126*, 299–312. [[CrossRef](#)]
- Hardy, P.; Cazzolato, B.S.; Ding, B.; Prime, Z. A Maximum Capture Width Tracking Controller for Ocean Wave Energy Converters in Irregular Waves. *Ocean Eng.* **2016**, *121*, 516–529. [[CrossRef](#)]

27. Lettenmaier, T.; Von Jouanne, A.; Brekken, T. A New Maximum Power Point Tracking Algorithm for Ocean Wave Energy Converters. *Int. J. Mar. Energy* **2017**, *17*, 40–55. [[CrossRef](#)]
28. Carandell, M.; Toma, D.M.; Holmes, A.S.; del Río, J.; Gasulla, M. Experimental Validation of a Fast-Tracking FOCV-MPPT Circuit for a Wave Energy Converter Embedded into an Oceanic Drifter. *J. Mar. Sci. Eng.* **2023**, *11*, 816. [[CrossRef](#)]
29. Yang, J. Research on Key Technologies of Horizontal Pendulum Wave Energy Converter. Ph.D. Thesis, Zhejiang University, Hangzhou, China, 2018.
30. Mishra, S.; Purwar, S.; Kishor, N. Maximizing Output Power in Oscillating Water Column Wave Power Plants: An Optimization Based MPPT Algorithm. *Technologies* **2018**, *6*, 15. [[CrossRef](#)]
31. Yao, G.; Luo, Z.; Lu, Z.; Wang, M.; Shang, J.; Guerrerob, J.M. Unlocking the Potential of Wave Energy Conversion: A Comprehensive Evaluation of Advanced Maximum Power Point Tracking Techniques and Hybrid Strategies for Sustainable Energy Harvesting. *Renew. Sustain. Energy Rev.* **2023**, *185*, 113599. [[CrossRef](#)]
32. Yue, X.; Zhang, J.; Meng, F.; Liu, J.; Chen, Q.; Geng, D. Multi-Timescale Lookup Table Based Maximum Power Point Tracking of an Inverse-Pendulum Wave Energy Converter: Power Assessments and Sensitivity Study. *Energies* **2023**, *16*, 6195. [[CrossRef](#)]
33. Dong, F.; Pan, S.; Gong, J.; Cai, Y. Comprehensive Wave-to-Wire Model and Control Strategy Design for Wave Energy Conversion System. *Ocean Eng.* **2023**, *284*, 115164. [[CrossRef](#)]
34. Sjolte, J.; Sandvik, C.M.; Tedeschi, E.; Molinas, M. Exploring the Potential for Increased Production from the Wave Energy Converter Lifesaver by Reactive Control. *Energy* **2013**, *6*, 3706–3733. [[CrossRef](#)]
35. Hansen, R.H.; Andersen, T.O.; Pedersen, H.C. Model Based Design of Efficient Power Take-off Systems for Wave Energy Converters. In Proceedings of the 12th Scandinavian International Conference on Fluid Power; Tampere University Press: Tampere, Finland, 2011; pp. 35–49.
36. Wu, S.; Liu, C.; Chen, X. Offshore Wave Energy Resource Assessment in the East China Sea. *Renew. Energy* **2015**, *76*, 628–636. [[CrossRef](#)]
37. Cargo, C.J.; Hillis, A.J.; Plummer, A.R. Strategies for Active Tuning of Wave Energy Converter Hydraulic Power Take-off Mechanisms. *Renew. Energy* **2016**, *94*, 32–47. [[CrossRef](#)]

Disclaimer/Publisher’s Note: The statements, opinions and data contained in all publications are solely those of the individual author(s) and contributor(s) and not of MDPI and/or the editor(s). MDPI and/or the editor(s) disclaim responsibility for any injury to people or property resulting from any ideas, methods, instructions or products referred to in the content.